REPORT DOCUMENTATION PAGE

Form Approved OMB No. 0704-0188

Public reporting burden for this collection of information is estimated to average 1 hour per response, including the time for reviewing instructions, searching existing data sources, gathering and maintaining the data needed, and completing and reviewing this collection of information. Send comments regarding this burden estimate or any other aspect of this collection of information, including suggestions for reducing this burden to Department of Defense, Washington Headquarters Services, Directorate for Information Operations and Reports (0704-0188), 1215 Jefferson Davis Highway, Suite 1204, Arlington, VA 22202-4302. Respondents should be aware that notwithstanding any other provision of law, no person shall be subject to any penalty for failing to comply with a collection of information if it does not display a currently valid OMB control number. **PLEASE DO NOT RETURN YOUR FORM TO THE ABOVE ADDRESS.**

1. REPORT DATE *(DD-MM-YYYY)*	2. REPORT TYPE	3. DATES COVERED *(From - To)*
29-02-2008	Final	01-04-2006 - 30-11-2007

4. TITLE AND SUBTITLE

Effects of Leading Edge Film-Cooling and Surface Roughness on the Downstream Film-Cooling Along a Transonic Turbine blade for Low and High Free-Stream Turbulence

5a. CONTRACT NUMBER

5b. GRANT NUMBER
FA9550-05-1-0250

5c. PROGRAM ELEMENT NUMBER

6. AUTHOR(S)
Raben, Sam
Vlachos, Pavlos
Ng, Wing

5d. PROJECT NUMBER

5e. TASK NUMBER

5f. WORK UNIT NUMBER

7. PERFORMING ORGANIZATION NAME(S) AND ADDRESS(ES)
Wing Ng
Dept of Mechanical Engineering
Virginia Tech
Blacksburg VA, 24060

8. PERFORMING ORGANIZATION REPORT NUMBER
VT-ME-2008-AFOSR-1

9. SPONSORING / MONITORING AGENCY NAME(S) AND ADDRESS(ES)
John D. Schmisseur/NA
AFOSR - NA
875 N. Randolph St
Suite 325, Rm 3112,
Arlington, Va 22203

10. SPONSOR/MONITOR'S ACRONYM(S)
AFOSR

11. SPONSOR/MONITOR'S REPORT NUMBER(S)
N/A

12. DISTRIBUTION / AVAILABILITY STATEMENT
No Restriction

DISTRIBUTION STATEMENT A
Approved for Public Release
Distribution Unlimited

AFRL-SR-AR-TR-08-0163

13. SUPPLEMENTARY NOTES
None

14. ABSTRACT

This report is the culmination of a two year effort to demonstrate the capability for performing near wall high resolution Time Resolved Particle Image Velocimetry (TRDPIV) measurements in a transonic turbine. Performing TRDPIV in high speed wall bounded flows with high resolution/magnification often posses significant difficulties. For this reason, two preliminary studies where conducted in order to further understand the challenges that would be present in this type of environment. Hardware and algorithm advancements and developments ultimately enabled performing TRDPIV in the transonic cascade facility. However, high pressure, high speed and the turbine blade complex geometries (high curvature and acceleration) significantly inhibit our ability to deliver homogeneous distribution of flow tracers, especially in the near wall region resulting in low quality measurements and regions with randomly missing data. In addition to our experimental results this effort delivers a novel advanced data reconstruction methodology based on proper orthogonal decomposition that was developed to overcome the aforementioned limitation. The following report documents in detail the methods and results generated throughout this effort.

15. SUBJECT TERMS
Turbine Blade, Film-Cooling, Free-Stream Turbulence

16. SECURITY CLASSIFICATION OF: NONE			17. LIMITATION OF ABSTRACT	18. NUMBER OF PAGES	19a. NAME OF RESPONSIBLE PERSON
a. REPORT	b. ABSTRACT	c. THIS PAGE	UU	62	Wing Ng
					19b. TELEPHONE NUMBER *(include area code)* 540-231-7274

EFFECTS OF LEADING EDGE FILM-COOLING AND SURFACE ROUGHNESS ON THE DOWNSTREAM FILM-COOLING ALONG A TRANSONIC TURBINE BLADE FOR LOW AND HIGH FREE-STREAM TURBULENCE

BY SAM RABEN, PAVLOS VLACHOS WING NG

VIRGINIA TECH MECHANICAL ENGINEERING DEPARTMENT

BLACKSBURG, VA 24060

TO: TECHNICALREPORTS@AFOSR.AF.MIL

SUBJECT: FINAL PROGRESS STATEMENT TO JOHN SCHMISEUR

CONTRACT/GRANT #: FA9550-06-1-0250

REPORTING PERIOD: APRIL 1, 2006 - NOVEMBER 30, 2007

ACCOMPLISHMENTS (200 WORDS):

This report is the culmination of a two year effort to demonstrate the capability for performing near wall high resolution Time Resolved Particle Image Velocimetry (TRDPIV) measurements in a transonic turbine. Performing TRDPIV in high speed wall bounded flows with high resolution/magnification often posses significant difficulties. For this reason, two preliminary studies where conducted in order to further understand the challenges that would be present in this type of environment. Hardware and algorithm advancements and developments ultimately enabled performing TRDPIV in the transonic cascade facility. However, high pressure, high speed and the turbine blade complex geometries (high curvature and acceleration) significantly inhibit our ability to deliver homogeneous distribution of flow tracers, especially in the near wall region resulting in low quality measurements and regions with randomly missing data. In addition to our experimental results this effort delivers a novel advanced data reconstruction methodology based on proper orthogonal decomposition that was developed to overcome the aforementioned limitation. The following report documents in detail the methods and results generated throughout this effort.

ARCHIVAL PUBLICATIONS (PUBLISHED) DURING REPORTING PERIOD: NONE

CHANGES IN RESEARCH OBJECTIVES: NONE

CHANGE IN AFOSR PROGRAM MANAGER: NONE

EXTENSIONS GRANTED OR MILESTONES SLIPPED: NONE

20080404112

CONTENTS

Contents **2**

1. Introduction **4**

2. Low Speed Tests: **5**

2.A. Introduction 5

2.B. Nomenclature 5

2.C. Experimental Methodology 6

2.C.I Experimental Facility 6

2.C.II Instrumentation 8

2.C.III Inlet and Test Conditions 9

2.D Results 9

3. Gappy Data Reconstruction: **18**

3.A. Introduciton: 18

3.B. Nomenclature: 19

3.C. Proper Orthogonal Decomposition and Reconstruction Methodology: 19

3.C.I DNS Data and Data Removal: 19

3.C.II Proper Orthogonal Decomposition: 20

3.C.III Everson - Sirovich Method 21

3.C.IV Venturi - Karniadakis Method 22

3.D. Convergence Criteria 23

3.D.i Everson – Sirovich Method 23

3.D.II Venturi – Karniadakis Method 23

3.D.III Continuity Based Convergence Criteria (CBCC) 25

3.E. Results 26

3.E.I Gappy Percentage and Size Results 26

3.E.II Field Error Analysis 31

3.F Conclusions 33

4. Wall Jet 34

4.A. Introduction 34

4.B. Nomenclature 35

4.C. Experimental Setup 35

4.D. Proper Orthognal Decomposition 37

4.E. Vortex Identification 39

4.F. Results and Discussion 40

4.F.I Time Averaged Analysis 40

4.F.II Proper Orthogonal Decomposition: 41

4.F.III Vortex Identification on POD Reduced Fields 46

4.G. Conclusion 47

5. High Speed Cascade Experiment 49

5.A. Introduction 49

5.B. Experimental Setup 49

5.C. Results 53

5.D. Conclusions 57

6. Conclusions and Future Work 58

7. References 59

1. INTRODUCTION

The aim of this effort was to understand the physical requirements as well as methodology required in order to employ Time Resolved Digital Particle Image Velocimetry (TRDPIV) for measuring the interaction of large scale turbulent structures with the near wall flow of turbine blades in a transonic cascade facility. Previous attempts to perform measurements such as this have been unsuccessful because of both limitations in equipment as well as proper methodology for acquisition and processing of the data. This work addresses those issues and successfully demonstrates a proof-of-concept experiment in a transonic wind tunnel at Virginia Tech.

The first preliminary test was a large scale low speed wind tunnel study that matches loading conditions of the full scale transonic tunnel. This study successfully demonstrated, at a reduced flow speed, the ability to not only perform measurements with kHz sampling but also to track large scale structures and their interaction with the stagnation region of a turbine blade. A second preliminary test, of a developing wall jet, was also undertaken during this work. This experiment helped in demonstrating the capability of taking high speed high magnification TRDPIV measurements. The Reynolds number ranged for this experiment from 150 – 10,000 which corresponded to velocities of 1 - 80 m/s.

From previous experiments it was established that flow tracer delivery is not a trivial task in a high speed high back pressure tunnel. Any PIV measurement requires uniform spatial seeding density, but time-resolved measurements require uniform temporal seeding density as well. To this end, a high pressure particle generator was developed. This advancement enhanced our capability beyond what was previously attainable. Unfortunately, this was not sufficient to resolve the issue of seeding all together, and an advanced data reconstruction methodology was developed to reconstruct areas of the flow field that where lost do to inhomogeneous seeding. This reconstruction methodology, based on Proper Orthogonal Decomposition (POD), has been shown to produce errors in corrected velocities below tradition spatial techniques alone. The combination of both particle generator and reconstruction methodology would be instrumental for successfully delivering TRDPIV measurements in a transonic wind tunnel facility.

The culmination of this research was a demonstration of TRDPIV measurements inside of a transonic wind tunnel. While the results of this experiment served primarily as a proof-of-concept, they positively demonstrate the capability of performing such measurements in a high speed high pressure environment which to the best of our knowledge has never successfully been achieved before. This report documents in detail each of these preliminary experiments as well as the development of a methodology required for these measurements to be successful.

2. LOW SPEED TESTS:

2.A. INTRODUCTION

This section of the report describes results from a proof-of-concept study to perform time-resolved flow field measurements in a turbine cascade using digital particle image velocimetry (DPIV). The results described here were generated in a large-scale low speed tunnel at Virginia Tech. Measurement capabilities developed in this concept study will be applied to a high-speed transonic cascade at Virginia Tech, so that simultaneous measurements of surface heat transfer and spatio-temporally resolved flow fields can be acquired.

The specific tasks of the original proposed work are listed below.

Task 1: *Demonstrate that time resolved DPIV measurements deliver temporal resolution sufficient to resolve flow field structures with kHz time scales.*

Task 2: *Demonstrate that time resolved DPIV measurements deliver spatial resolution sufficient to resolve the interaction of large scale turbulence with the boundary layer on the surface of the blade.*

Task 3: *Explore how close we can measure the velocity field near the blade surface in order to resolve the boundary layers and the inherent eddies.*

2.B. NOMENCLATURE

C	True chord of stator vane
C_{ax}	Axial chord of stator vane
DPIV	Digital Particle Image Velocimetry
LDV	Laser Doppler velocimetry
P	Pitch of stator vane
Re_{in}	Inlet Reynolds number, $\mathrm{Re}_{\mathrm{in}} = \mathrm{CU}_{\mathrm{in}}/\nu$
S	Span of stator vane
Tu	Inlet turbulence intensity, relative to U_{in} = 6.3 m/s
$\overline{u'v'}$	Reynolds stresses

X, Y, Z Coordinate directions (streamwise, pitchwise, spanwise)

U Streamwise velocity (aligned with X)

V Pitchwise velocity (aligned with Y)

2.C. EXPERIMENTAL METHODOLOGY

The facility used to perform Time-Resolved DPIV measurements will be described first, followed by a discussion of the DPIV and Laser Doppler instrumentation and data acquisition techniques. Finally, the test conditions for this proof-of-concept study will be presented.

2.C.I EXPERIMENTAL FACILITY

Time-Resolved Digital Particle Image Velocimetry (TR-DPIV) measurements were taken in the large low-speed wind tunnel at Virginia Tech. This facility allows for high-resolution measurements at Reynolds numbers that match gas turbine engine conditions, although engine Mach numbers are not matched. However, the intent of the tunnel design is to provide for high spatial resolution of turbine heat transfer, which has been shown to be relatively independent of Mach number, up to shock development. The closed-loop tunnel, depicted in Figure 1, is driven by an axial fan. The flow can be split into a primary path and two secondary paths, located above and below the primary path. The secondary paths are used to supply air for dilution or film cooling flow. In this study, the high-momentum dilution jets used to generate freestream turbulence were supplied by air from the secondary flow paths.

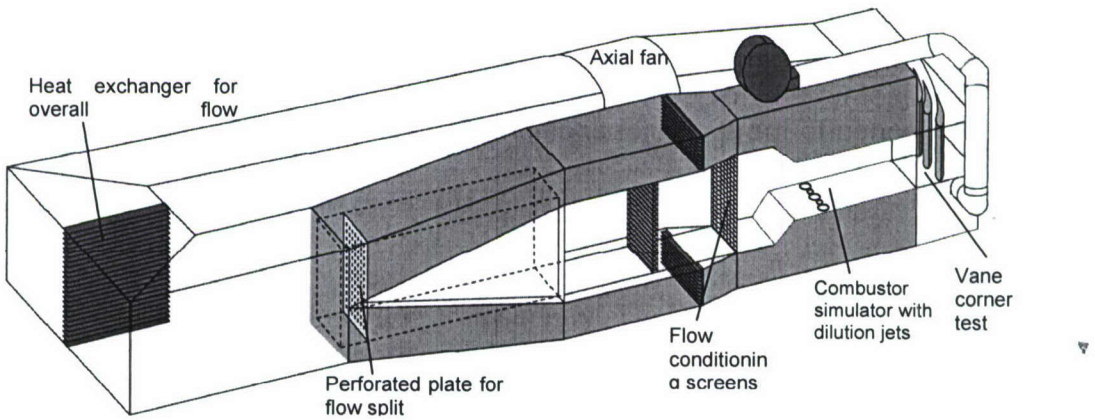


Figure 1. An illustration of the large-scale low-speed tunnel with vane corner test section.

After encountering the split, the primary flow passes through several conditioning screens and enters a contraction section, with 45° symmetric contractions on the top and bottom of the section. The tunnel flow area remains constant downstream of the contraction, up to the inlet of the vane test section. The vane test section consists of one full vane and two half vanes, comprising two full vane flow passages as seen in

Figure 2. The vanes are a linear extrusion of the midspan section of a PW6000 turbine engine nozzle guide vane, scaled by a factor of 9 for high measurement resolution. Table 1 lists the geometric parameters of the vane. A flexible wall, as well as bleeds and tailboards, ensure that the flow is symmetric through the two passages. Surface static pressure taps around the periphery of the center vane allow for measurement of the vane static pressure coefficient, for correct positioning of the flexible wall and the bleeds.

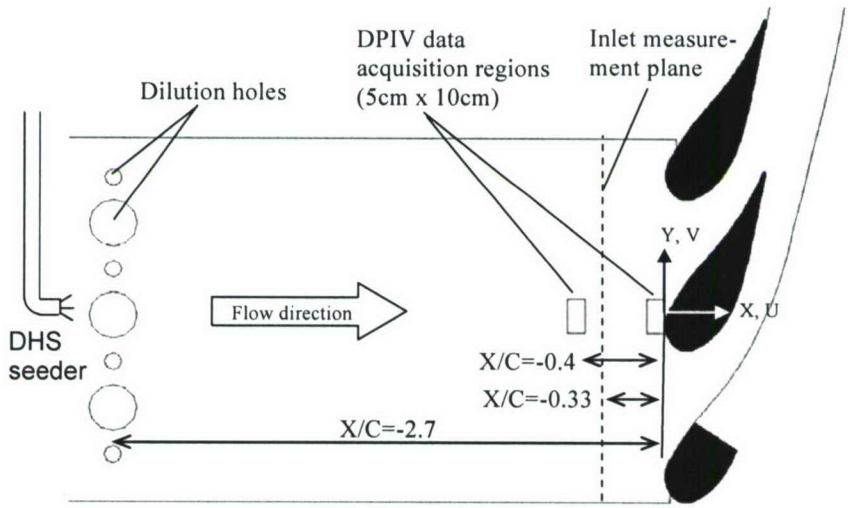


Figure 2. A top view of the combustor simulator and vane test section, as well as the DPIV data acquisition areas.

Table 1. Vane Geometry and Flow Conditions

Parameter	Dimension
Scaling factor	9
Scaled vane chord (C)	59.4 cm
Axial chord/chord (C_{ax}/C)	0.48
Pitch/chord (P/C)	0.77
Span/chord (S/C)	0.93
Inlet Reynolds number (Re_{in})	$2.2x10^5$
Inlet mainstream velocity (U_{in})	6.3 m/s
Inlet, exit angle	0°, 78°
Inlet, exit Mach number	0.017, 0.085

Freestream turbulence was generated by cross-stream injection of high-momentum jets into the primary flow path through simulated combustor liner dilution holes placed upstream of the vane test section, as illustrated in Figure 2. The dilution jet geometry and layout were developed for other studies in this wind tunnel, and were based on realistic turbine engine geometries. Two different dilution hole diameters were used to generate jets injected perpendicular to the primary flow path direction. The holes were placed in an alternating pattern in the pitchwise direction on the top and bottom walls of the tunnel at 2.7 vane chords upstream of the vane stagnation location. Jets were individually controlled by valves to ensure uniform jet momentum flux ratios.

2.C.II INSTRUMENTATION

A two-component Laser Doppler Velocimeter (LDV) was placed above the test section to measure streamwise and pitchwise velocity components entering the cascade, as well as velocities at a point in the DPIV data field near the vane stagnation. A 350mm focusing lens on the LDV produced a measurement volume with a length of 1.3 mm and a diameter of 90 μm. For LDV measurements, the flow was seeded with 1 μm-diameter olive oil particles. The seed was injected directly upstream of the axial fan so that it would distribute evenly to the primary and secondary flow paths. Measured velocities were corrected for bias errors by the residence time weighting correction scheme. Each of the mean and rms velocities captured by the LDV were averaged over 10,000 points, which took nominally 20 seconds to acquire. For the coincident velocity measurement point close to the vane (used to compare with the DPIV data), 25,000 data points were obtained over a sampling time of approximately 35 seconds.

Digital Particle Image Velocimetry (DPIV) was also used to measure the flow field. A 50-watt laser illuminated a thin sheet of particles at the mid span of the vane. Using a series of lenses, the laser beam was made to be 1 mm in thickness and 5 cm in width. The selected field of view of 5 cm by 10 cm was a compromise between desired magnification (based on estimated Kolmogorov length scale of 100 μm) and field of view necessary to capture the turbulence integral length scale (expected to be of the order of the dilution jet diameter. The laser was directed into the side of the tunnel so that it illuminated the region upstream of the vane stagnation; see Figure 3. The laser was double-pulsed at 1 kHz and synchronized with a high speed camera for 6 seconds of data acquisition time. The double-pulse separation time was 100 μsec which allowed for particles to move approximately 8-10 pixels per pulse. Six thousand independent flow field measurements were acquired for each case. The high speed camera was a CMOS digital camera with a resolution of 1280 x 524 pixels. It was determined that the camera should be placed at an angle to capture the most scattered light from particles in the laser plane. Dewarping of the off-axis image to obtain correct streamwise and pitchwise velocities was performed with the use of a calibration plate and software provided by LaVision. The flow was seeded with 1 μm-diameter olive oil particles, as well as 1-5 μm-diameter Diethyl Hexal Sebacate (DHS) particles. The olive oil seed was the same seed used for the LDV and was injected as mentioned above. The DHS

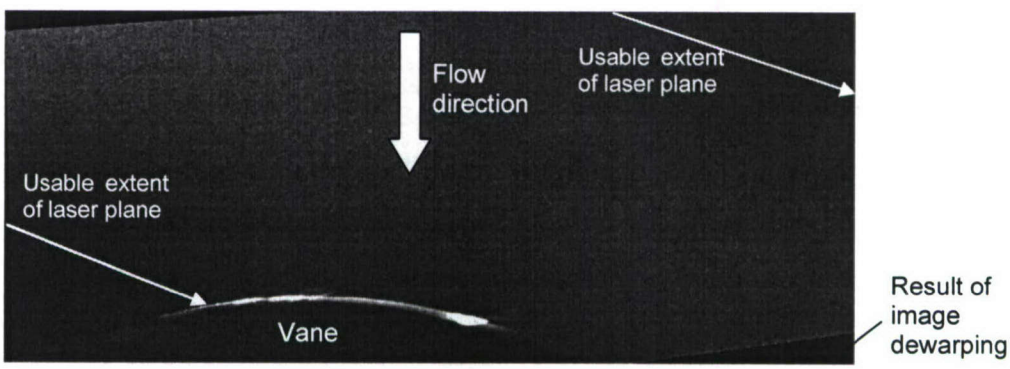


Figure 3. A DPIV image of seeded flow at the vane stagnation region, for the 19% Tu case.

was injected upstream of the dilution jets via a tube inserted into the flowpath, so as to maintain a densely seeded flowfield in the PIV acquisition region.

2.C.III INLET AND TEST CONDITIONS

The velocity and turbulence levels entering the vane cascade were characterized at 0.33 vane chords upstream of the vane stagnation with the LDV. Figure 4 presents pitchwise profiles of velocity components entering the cascade for the two freestream turbulence levels tested in this study. Note that the results are non-dimensionalized by the nominal average inlet velocity to the cascade (U_{in}) of 6.3 m/s.

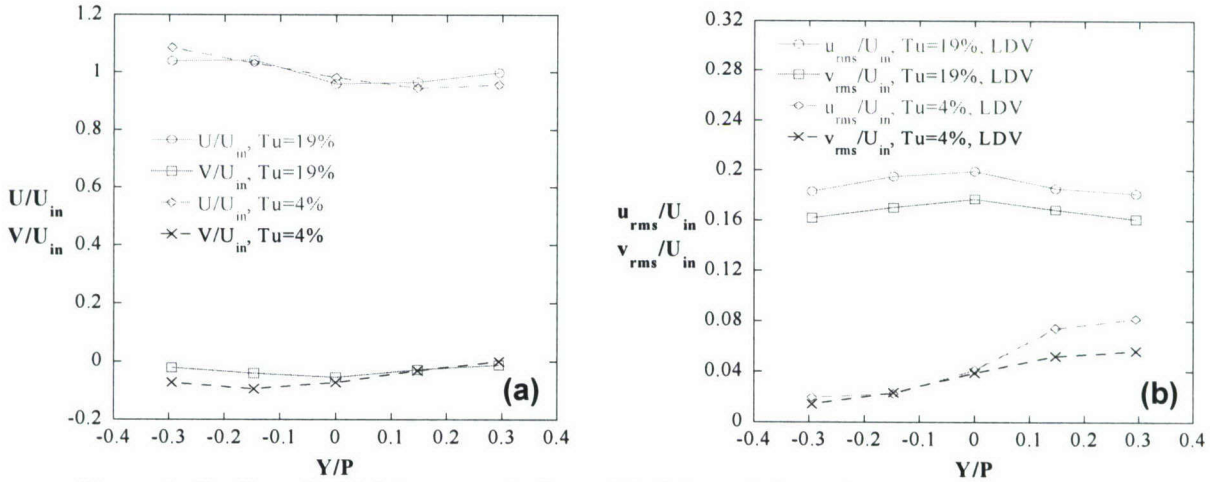


Figure 4. Profiles of (**a**) inlet mean velocity and (**b**) inlet turbulence levels, measured at X/C=-0.33 upstream of the vane stagnation.

Two streamwise turbulence levels were obtained for this study so that the spatio-temporal resolution of the DPIV system could be tested. The turbulence levels quoted in this study are the pitchwise average of the measured local turbulence levels across the vane pitch (from vane to vane) at X/C=-0.33 upstream of the vane stagnation. A streamwise turbulence level of 19% was obtained by opening the small and large dilution holes. For the lower turbulence level of 4%, the dilution jets were closed, but the DHS seeder injection tube was left in the flowpath, since the additional seed was necessary to obtain enough particles for the DPIV images. This is the reason that turbulence levels are less uniform across the pitch for 4% Tu. At each turbulence level, DPIV measurements were taken both at the vane stagnation, and at a location 0.4 vane chords upstream of the vane. Table 2 lists the test matrix for this study.

Table 2. DPIV Test Matrix for Large-Scale Low-Speed Tunnel

Location	Turbulence level	
Midspan, vane stagnation (X/C=0, Y/P=0, Z/S=0.5)	**19%**	**4%**
Midspan, cascade inlet (X/C=-0.4, Y/P=0, Z/S=0.5)	**19%**	**4%**

2.D RESULTS

The results presented here are organized according to the proposal tasks listed in the Introduction.

Task 1: *Demonstrate that time resolved DPIV measurements deliver temporal resolution sufficient to resolve flow field structures with kHz time scales.*

To test the temporal resolution of the DPIV system, flowfield measurements were taken at 1 kHz using the single-exposure double-pulsed laser technique described earlier. Figure 5 presents a sequence of instantaneous vorticity contours around the vane stagnation, for the 19% inlet Tu level. A noticeable region of high positive vorticity is convected from the top left corner of Figure 5a toward the vane in subsequent timesteps. Other regions of high-magnitude vorticity (both negative and positive) are also convected through the flowfield.

Task 2: *Demonstrate that time resolved DPIV measurements deliver spatial resolution sufficient to resolve the interaction of large scale turbulence with the boundary layer on the surface of the blade.*

Full field measurements of the flow around the vane stagnation point were obtained with the DPIV system and compared to the results of Radomsky & Thole [1], who used the same vane geometry. Figure 6 presents contours of time-averaged results for streamwise (U) and pitchwise (V) velocities around the vane stagnation point. Time-averaged streamwise velocity contours are similar for the DPIV measurements at both turbulence levels tested in this study, and also compare well to Radomsky & Thole. Note a slight difference in pitchwise velocity between the DPIV measurements in Figures 6b and 6d, and Radomsky & Thole's measurements in Figure 6f. For pitchwise velocity measurements on the pressure side of the stagnation point (above Y/C=0), velocity levels are about 0.1 V/U_{in} lower than those measured by Radomsky & Thole. Figure 8 shows streamlines calculated for the 19% Tu and 4% Tu cases, overlaid with streamlines calculated from Radomsky & Thole. It is apparent that on the pressure side of the vane stagnation (above Y/C=0), the DPIV measurements show less pitchwise turning of the flow than Radomsky & Thole's measurements. Note that in general, a stagnation streamline has some slight pitchwise velocity as it approaches the vane. Streamlines on the pressure side of the stagnation streamline tend to have little or no pitchwise velocity component until close to the vane. The small pitchwise velocity for these streamlines, relative to the higher streamwise velocity, may be difficult for the DPIV system to accurately resolve at the short double-pulsing separation time of 100 μsec used in this study, and more studies are planned to account for this.

For a quantitative validation of the DPIV system, velocity components are also plotted in Figure 7 along a line beginning at the vane stagnation point and extending upstream along the X-coordinate direction. Again, from Figure 7b we can see that the DPIV measurements show slightly more negative pitchwise turning (i.e., less turning toward the pressure side) than Radomsky & Thole, near the vane stagnation. However, note that the trends are similar, and the DPIV measurements taken upstream agree well with the trend of Radomsky & Thole.

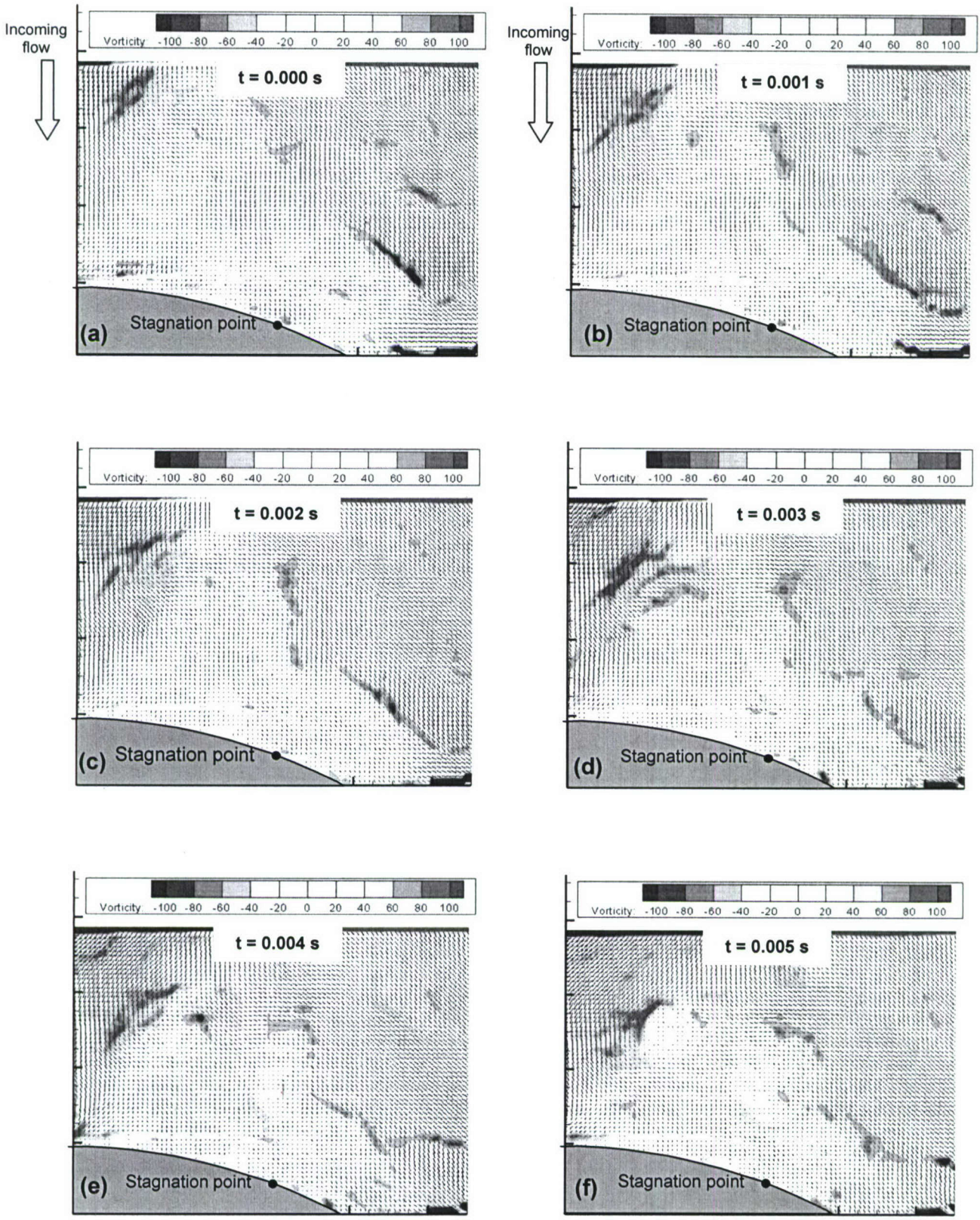


Figure 5. Contours of vorticity plotted for consecutive timesteps **(a)-(l)** (continued on next page).

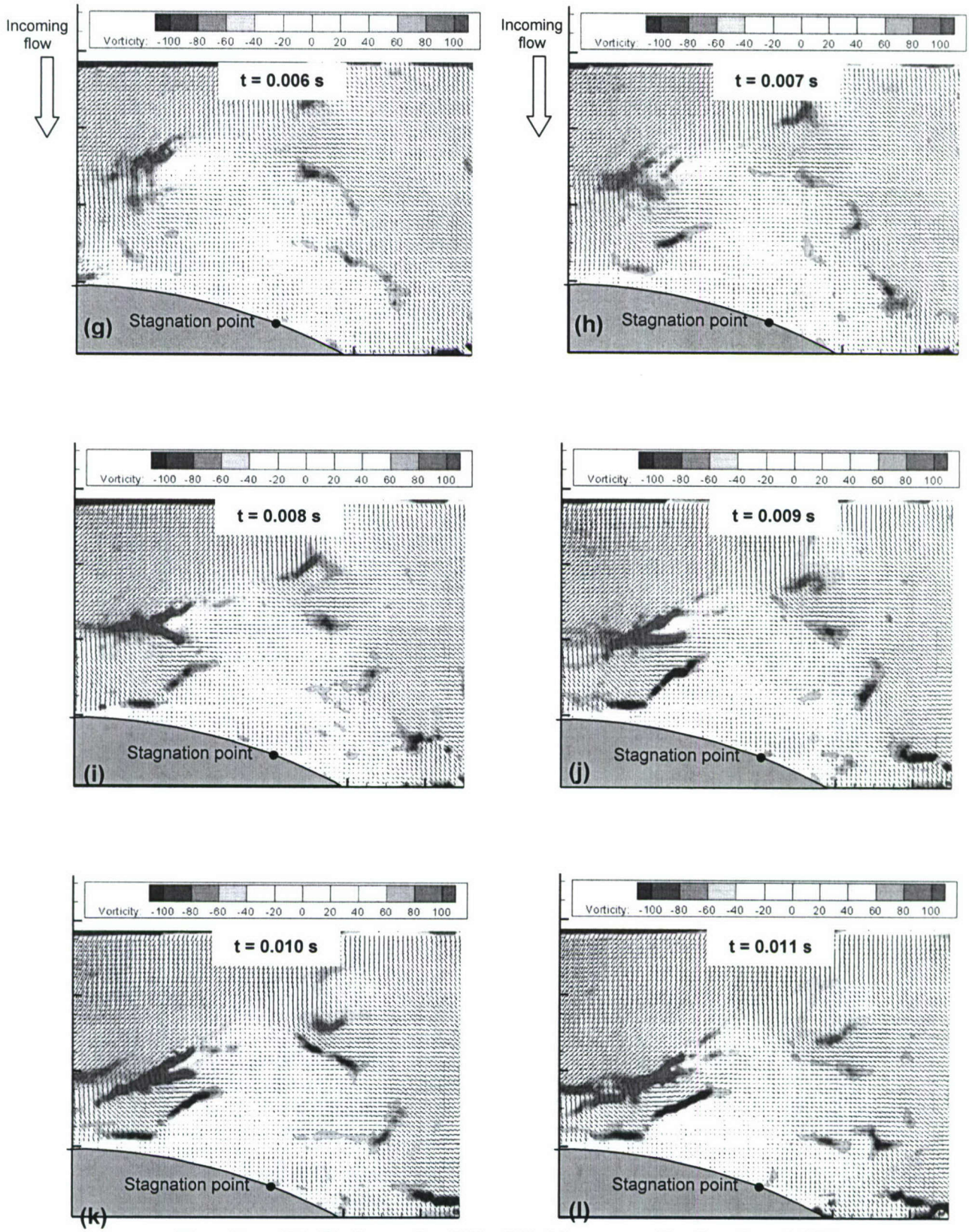


Figure 5, cont'd. Contours of vorticity plotted for consecutive timesteps **(a)-(k)**.

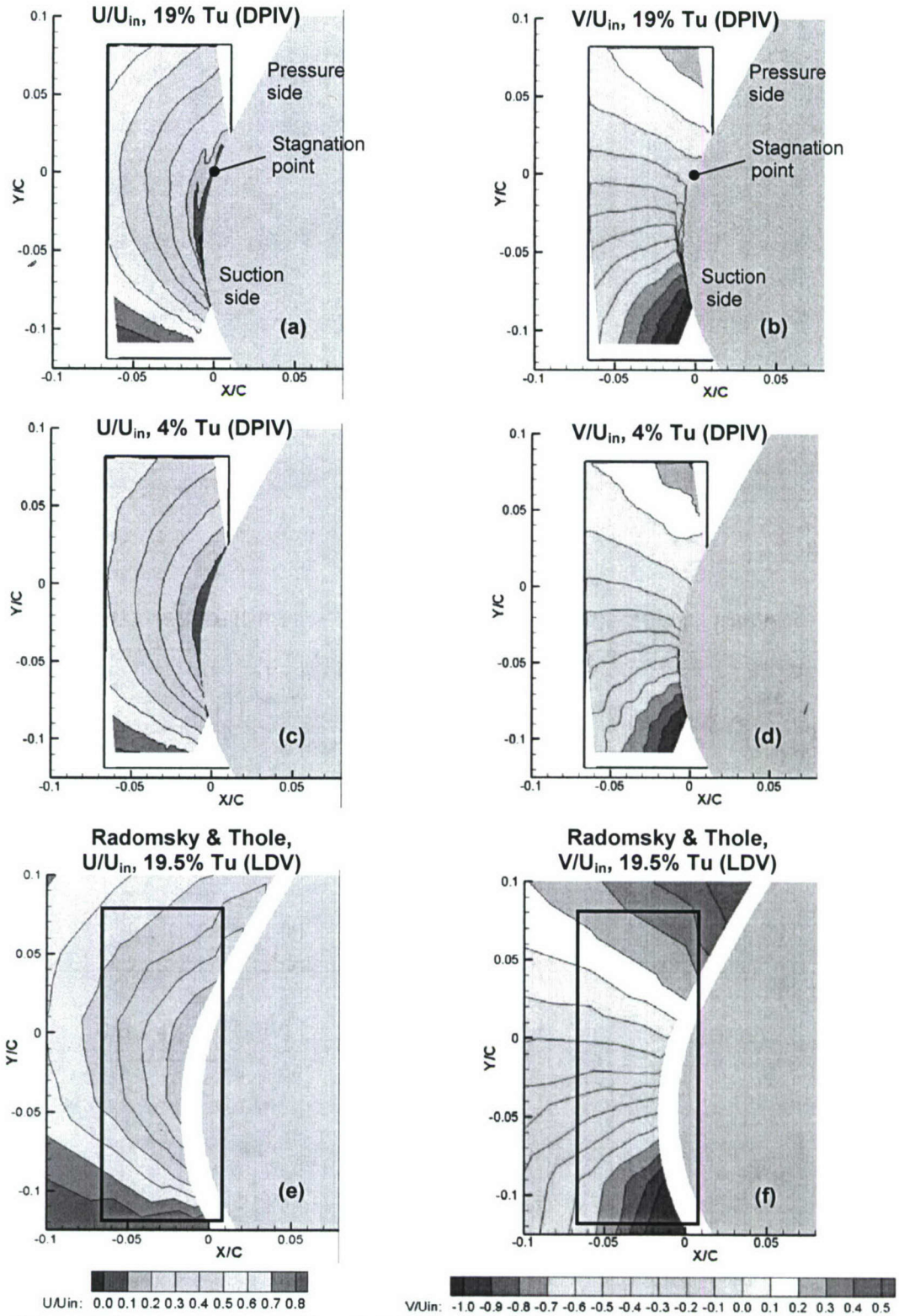


Figure 6. Mean streamwise (U) and pitchwise (V) velocity measurements at the vane stagnation, obtained with the DPIV system for 19% Tu (**a, b**) and 4% Tu (**c, d**), compared to Radomsky & Thole at 19.5% Tu (**e, f**) [1].

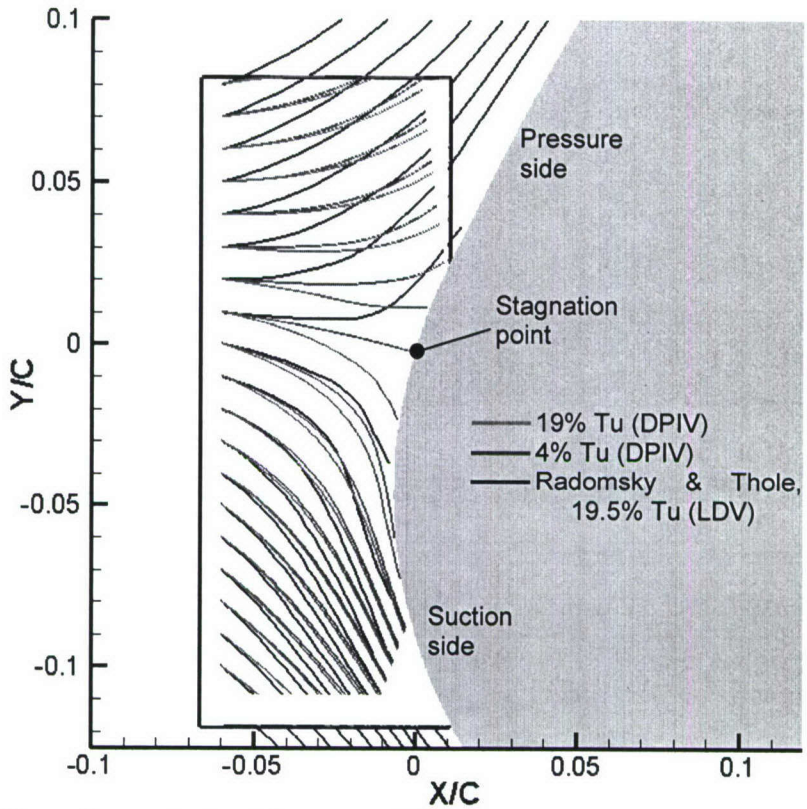


Figure 8. Streamlines calculated from mean DPIV velocity measurements at 19% and 4% inlet Tu, compared to streamlines calculated from Radomsky & Thole at 19.5% Tu [1].

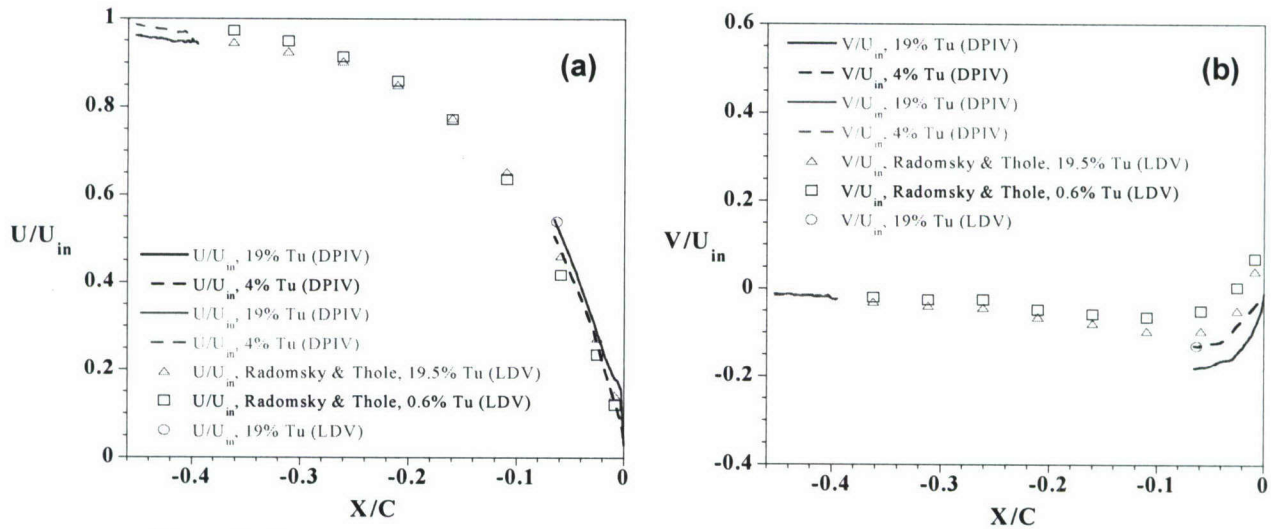


Figure 7. Streamwise (**a**) and pitchwise (**b**) mean velocities along a line extending upstream from the vane stagnation.

The RMS of the velocity fluctuations at the 19% inlet turbulence level are shown in Figure 10, along the line extending upstream of the vane stagnation. Note that the streamwise velocity fluctuations (u_{rms}) have a lower magnitude and less of a rapid increase around X/C=-0.03 as the vane is approached, for the DPIV measurement versus Radomsky & Thole. This disagreement could be caused by the lack of sufficient laser intensity, which was a result of the wide field of view needed in this study and the difficulty of densely seeding the flow. Also, note that the freestream turbulence generation method is different between this study (dilution jets) and that of Radomsky & Thole (a grid far upstream of the vane). In Figure 10, the pitchwise velocity fluctuations (v_{rms}) measured by the DPIV system agree well with Radomsky & Thole's measurements, for locations very close to the vane stagnation. Lesser agreement is found upstream of X/C=-0.05, where the DPIV system shows higher fluctuating pitchwise velocities than Radomsky & Thole.

Figure 9 compares contours of normalized Reynolds stresses for DPIV measurements in this study at 19% Tu, to Radomsky & Thole at 19.5% Tu. Although the contour shapes of the two data sets do not seem to have many similarities, the magnitudes of Reynolds stresses upstream of the vane are similar. This is illustrated further by Figure 11, which shows normalized Reynolds stresses in the pitchwise direction, at a constant streamwise (X/C=-0.06) location. At this location upstream of the vane, DPIV Reynolds stress measurements show a similar trend to Radomsky & Thole's findings.

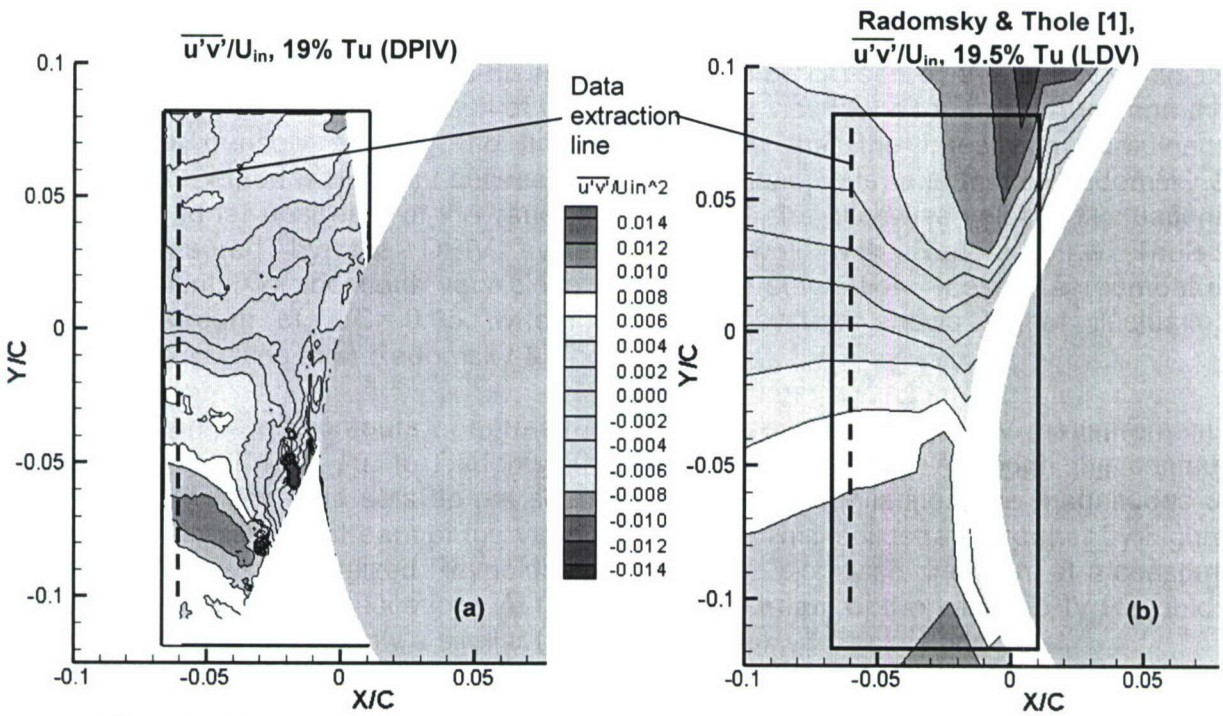


Figure 9. Contours of normalized Reynolds stresses for (**a**) DPIV measurements at 19% Tu, and (**b**) Radomsky & Thole [1] at 19.5% Tu.

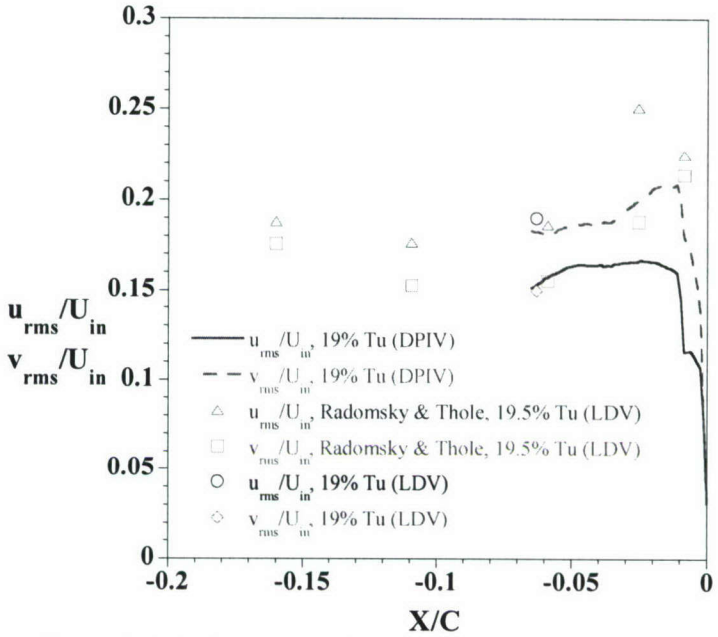


Figure 10. Streamwise and pitchwise velocity fluctuations along a line extending upstream from the vane stagnation.

Task 3: *Explore how close we can measure the velocity field near the blade surface in order to resolve the boundary layers and the inherent eddies.*

In order to achieve sufficient intensity around the vane stagnation, the laser plane could not illuminate much of the suction side of the vane. A shadowing effect of the vane geometric stagnation limited light intensity on the airfoil pressure side; i.e., the laser could not illuminate much of the pressure side of the vane since it was blocked. These effects did not allow us to achieve high-resolution measurements near the vane surface, for locations away from the stagnation point. Note that the stagnation point is theoretically the starting location of the vane surface boundary layer, so the region of valid DPIV data around the stagnation point was in a location of extremely small boundary layer thickness. The expected boundary layer thickness would be less than 0.001C (594 μm), based on boundary layer measurements taken by Radomsky & Thole [2] at locations farther along the pressure and suction surfaces of the airfoil. The magnification of the DPIV system (at 91.6 μm/pixel) would provide approximately six pixels in the boundary layer, but cross-correlation of the PIV image pairs results in a single measurement per 4 or 8 pixels. Higher magnification will probably be necessary to resolve the boundary layer near the vane stagnation. However, at a distance s/C = 0.15 from the vane stagnation along the pressure side, Radomsky & Thole [2] measured a boundary layer thickness of δ/C = 0.0034, which would correspond to 22 pixels (4-6 data points) at the same magnification of 91.6 μm/pixel.

Examination of Figure 3 shows another issue that may be detrimental for near-wall flow field measurements. Laser plane reflections from the surface of the vane made data very close to the vane unusable (low signal-to-noise ratio). The vane was painted flat black to minimize reflections, but as Figure 3 shows, the flat black paint did not

completely attenuate the reflections. Sufficient laser intensity in the rest of the field of view may help to lessen the effect of the reflections, or more likely, a new laser delivery technique needs to be developed.

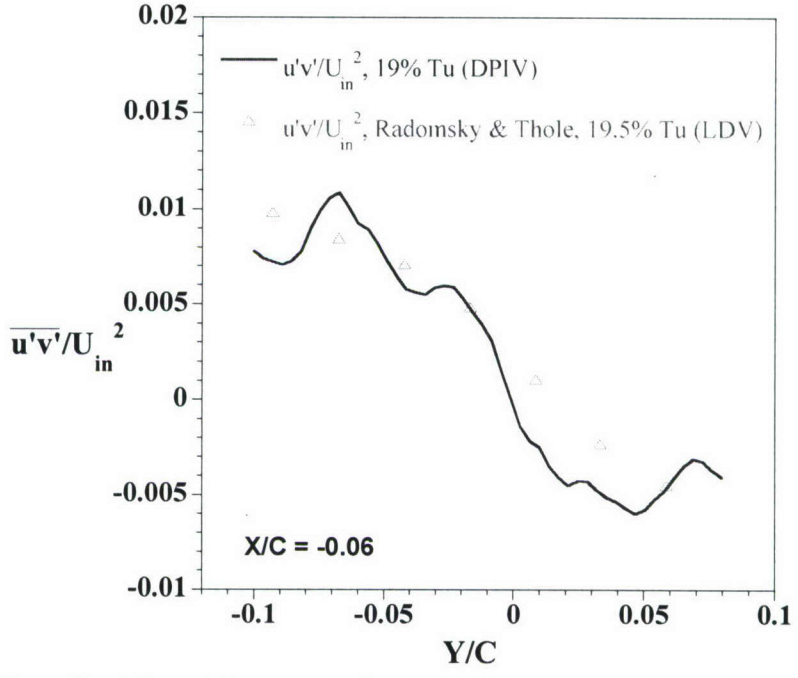


Figure 11. Normalized Reynolds stresses along a pitchwise line at X/C = -0.06 (see Figure 10).

3. GAPPY DATA RECONSTRUCTION:

Due to difficulties associated with measurements made in a high back pressure transonic cascade tunnel an advanced data reconstruction methodology was developed and implemented. The method utilizes Proper Orthogonal Decomposition to determine the correct values of missing data.

3.A. INTRODUCITON:

Erroneous measurements, data recovery, and reconstruction are common with almost all experimental data sets [3]. With the growth of techniques such as Particle Image Velocimetry (PIV) or Magnetic Resonance Velocimetry (MRV), data is recorded with high spatiotemporal resolution [4]. Such data sets are always subject to experimental error as well as processing error and therefore usually need validation [5, 6]. Advancements in PIV processing has helped to reduce errors due to correlations, but inhomogeneous seeding and varying image intensity will still produce incorrect vectors [7-9]. The most common form of validation is a simple linearly weighted spatial validation where individual vectors are compared with their neighbors and, if needed, replaced by a linear combination of those surrounding vectors [9]. Simple temporal as well as advanced nonlinear temporal validation methods have also been implemented [10]. While both methods help to produce higher accuracy data, their independence from each other limits their effectiveness. For temporal validation to be effective the time scale of the validation window must be on the same order as the scale of physical events in the flow. More advanced spatial validation methods have been developed such as Kriging, which is a form of linear least squares estimator but again does not contain any temporal information in its replacement [11].

With the growth of computational power, more advanced validation techniques are becoming feasible. Proper Orthogonal Decomposition (POD) is a mathematical method for producing low order representations of higher order systems. Properly calculated, these lower order representations have been shown to produce better estimations of the missing data even, compared to spatial techniques such as Kriging [12-15]. Everson and Sirovich first proposed the idea of using POD to reconstruct missing or "Gappy" data in 1995 [13]. Here, images of a face were reconstructed using two different methods. The first method was a reconstruction based on information from a complete solution and the second was a method independent of the 'true' solution. Following this, Venturi and Karniadakis advanced the methodology by producing an iterative procedure (V-K method) based on the Everson method that reduced error by an order of magnitude [15]. Their method, however, depended on knowledge of the 'true' or complete field, which renders the implementation impractical for validation of experimental fields. The work described herein proposes an approach for taking advantage of the V-K method without any *a priori* information about the true solution.

3.B. NOMENCLATURE:

$M(x,y;t)$	Mask locating correct (0) and bad data (1).
$U(\vec{x})$	Single Velocity field, (x,y) at a single time step.
$\phi(\vec{x})$	POD eigenfunction determined using Karhunen- Loéve Decomposition.
λ	Eigenspetra produced from POD.
$\phi^{(s)}$	POD eigenfunction determined using method of snapshots
$\alpha^{(s)}$	Projection coefficient associated with the method of snapshots
$\langle\cdot\rangle_t$	Ensemble average over time
$\|\cdot\|_2$	L2 normalization, square root of the sum of the squares.
$\|\cdot\|_\infty$	Maximum point wise value.

3.C. PROPER ORTHOGONAL DECOMPOSITION AND RECONSTRUCTION METHODOLOGY:

3.C.I DNS DATA AND DATA REMOVAL:

In order to test the proposed methodology, data from a DNS simulation of a turbulent boundary layer was used [16]. This data chosen due to their high spatio-temporal resolution correspond to artificial PIV image from the 2005 PIV challenge [16] therefore serving as an excellent benchmark case. The resolution per vector was 0.195 wall units, with a Reynolds number of 640. The Reynolds number was based on frictional velocity and channel half height. The temporal resolution was adjusted such that out-of-plane motion was one-half the laser plane thickness. Additional information on the experimental parameters can be found in Stanislas et al [16].

Starting with a complete flow field, noise was added to simulate errors common to PIV and MRV measurements. The noise values were randomly generated and range from 0-5% of the U and V velocity scale. The noise was normally distributed with zero bias and standard deviations of 0.1 and 0.005 for U and V respectively. Normally distributed noise is common in PIV results [9]. Next, random pieces of data were removed to create the "Gappy" flow field. Fields with 5%, 11%, 20%, 50%, and 80% gappyness were produced with gap sizes of 1x1, 3x3, 5x5, and NxM. For NxM gap sizes, data was removed in random rectangular shapes with sizes ranging from 1 to 5. This approach

explores the effectiveness of the method against isolated as well as clustered bad vectors. Therefore we simulate experimental measurements where gaps of clusters of bad vectors resulting from loss of correlation because of insufficient seeding or poor signal-to-noise, will be of variable sizes and shapes.

While bad vector detection is of equal importance to vector replacement, it is beyond the scope of this report. Here, it will be assumed that all bad vectors have been correctly identified and only good measurements remain. Locations of all bad points will be stored as shown by Equation 1. This is the same assumption made by Everson et al and Venturi et al for their reconstruction [13, 15].

$$M(x,y;t) = \begin{cases} 1 \text{ for locations of correct data} \\ 0 \text{ for locations of missing data} \end{cases} \tag{1}$$

Figure 12 shows the four different phases of the reconstruction process: true initial field, gaps are created, their corresponding mask is obtained, the field is reconstructed.

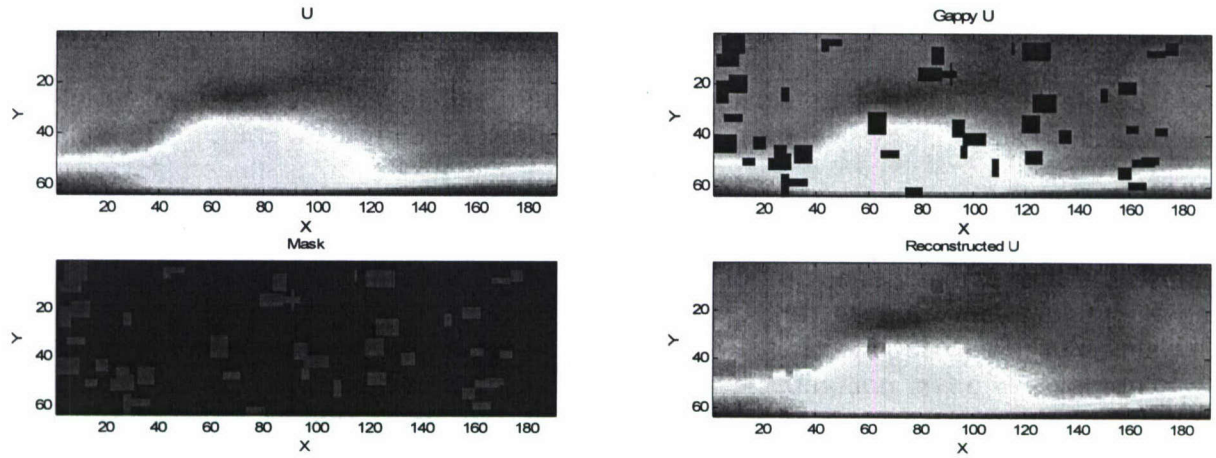


Figure 12. The Four stages of the data reconstruction: a) True field, b) Gaps are created in field, c) A mask is created of all of the gappy locations, d) The field is reconstructed using the Venturi - Karniadakis method.

For completeness, the basics of Proper Orthogonal Decomposition is described below, for more information please see [3, 13, 15, 17, and 18].

3.C.II PROPER ORTHOGONAL DECOMPOSITION:

The basic formulation of POD starts with the Fredhom Equation (2).

$$\int \left\langle U(\vec{x}) \otimes U(\vec{x}') \right\rangle \phi(\vec{x}') d\vec{x}' = \lambda \phi(\vec{x}) \tag{2}$$

To apply POD to discrete data, as would be done with PIV or MRV data, the equation must be discretized, as shown in equation 3. Here, $C_{i,j}$ is the two point correlation tensor which is an ensemble average over the total number of frames or snapshots, equation 4.

$$\sum_{p}\sum_{q} C_{i,j}(x,y;p,q)\phi_{j}^{(s)}(p,q) = \lambda\phi(x,y) \tag{3}$$

$$C_{i,j} = \left\langle U_i(x,y;t)U_j(x,y;t)\right\rangle_t \tag{4}$$

To minimize computation time, the method of snapshots is used [19]. The method assumes that the eigenfunctions created in equation 3 are a linear combination of the flow field snapshots multiplied by a corresponding projection coefficient.

$$\phi_j^{(s)}(x,y) = \sum_t \alpha^{(s)}(t)U_i(x,y;t) \tag{5}$$

Appling the method of snapshots, equation 5, to equation 3, a reduced eigenvalue problem is produced, equation 6.

$$\sum_n F_{n,l}\alpha^{(s)}(n) = \lambda^{(s)}\alpha^{(s)}(l) \tag{6}$$

$$F_{n,l} = \frac{1}{N}\sum_x\sum_y U_i(x,y;n)U_j(x,y;l) \tag{7}$$

Because of the orthogonality of the eigenfunctions, equation 5 can be rearranged to solve for the reconstructed flow field, where S is the number of snapshots used in reconstruction (8).

$$U_i(x,y;t) = \sum_t \alpha^{(s)}(t)\phi_j^{(s)}(x,y) \tag{8}$$

3.C.III EVERSON - SIROVICH METHOD

Both of the methods, Everson – Sirovich and Venturi – Karniadakis, described in this section base their reconstructions on the above POD procedure with changes only to the initial conditions and final reconstruction. The Everson – Sirovich (E-S) method for reconstruction consists of the following steps [13]:

a) Begin with time average values as initial guesses at M(x,y;t)=0 to produces $\hat{U}(x,y;t)$ for S number of snapshots;

b) Perform POD on $\hat{U}(x,y;t)$ to produce S spatial modes with corresponding projection coefficients;

c) Select N number of modes to use in reconstruction;

d) Using Equation 8, reconstruct the field using the determined number of modes;

$$U_N(x,y;t) = \sum_N \alpha^{(s)}(t)\phi^{(s)}(x,y)$$

Overwrite previous guess with the newly constructed field;
$\hat{U}(x,y;t) = U_N(x,y;t)$ only if $M(x,y;t)$

e) If the solution has converged stop, i.e. the eigenspectra has stopped changing, otherwise return to step b.

The condition for complete convergence for this method will be discussed later. This method has been shown to rely heavily on using the time averaged values as the initial condition [15]. Nevertheless, this method provides an optimal reconstruction without *a-priori* knowledge of the 'true' eigenspectrum of the field [3, 15].

3.C.IV VENTURI - KARNIADAKIS METHOD

Venturi and Karniadakis have proposed a method that is independent of initial guess as well as produces higher accuracy, based on the E-S method. For brevity this method will be referred to as the V-K method and consists of the following steps [15]:

a) Perform the standard E-S method employing only two modes (N=2) in the reconstruction;

b) Using the converged results from the previous step (N=2) as a new initial guess, repeat the E-S method now using 3 modes (N=3) in the reconstruction.

c) Proceed similarly for the nth iteration until the current section of the eigenspectrum stops changing.

In using the converged information from the previous mode, Venturi and Karniadakis have increased the resolvable number of modes by sometimes as much as an order of magnitude. This method is however more computationally expensive. Another drawback to the method is its lack of convergence criteria suitable for experimental data. This method requires knowledge of the true solution in order to achieve convergence.

It should be mentioned that there are a few limitations to both the E-S and V-K methods. Both methods cannot resolve an area obstructed in every snapshot [15]. While for symmetric fields this can sometimes be handled [20] this method in particular is not set

up to do so. These methods also have the constraint that a snapshot cannot be missing [15]. In either of these cases, reconstruction of the missing information is not possible.

3.D. CONVERGENCE CRITERIA

This section will discuss the convergence criteria for both the E-S method and V-K method as well as propose the use of the continuity equation to provide an experimental convergence criterion for the V-K method.

3.D.I EVERSON – SIROVICH METHOD

Venturi and Karniadakis, set forth a convergence criterion for optimal reconstruction for the E-S method such that it is applicable to experimental data [3, 15]. Convergence is determined by summing the eigenspectra produced from the method using different modes for reconstruction.

$$e_M = \frac{\sum_{j=1}^{N} \hat{\lambda}_{j(M)}^2}{\sum_{j=1}^{N} \lambda_j^2} \tag{9}$$

$$E_M = \sum_{j=1}^{N} \hat{\lambda}_{j(M)}^2 \tag{10}$$

With $\hat{\lambda}_{j(M)}^2$ being the jth eigenvalue from M-modes of reconstruction and λ_j^2 is jth eigenvalue from the 'true' solution. This equation will produce normalized results based on the 'true' solution. Using just the numerator, in Equation 10, a maximum value indicating the optimum resolvable mode will still be found corresponding to the optimum reconstruction. This selection is based on the notion that Equation 9 will approach the 'True' solution (e_m = 1) from the bottom without overshoot meaning that the maximum value of the numerator, (Equation 10), will represent the optimum reconstruction. Figure 13 shows equation 10 applied to 11% 3x3 gappy DNS data. It can be seen that the maximum number of resolvable modes for this method is 4. Using this number of modes does not produce the lowest reconstruction error. Errors in reconstruction will be discussed in the Results section.

3.D.II VENTURI – KARNIADAKIS METHOD

Venturi and Karniadakis demonstrated the maximum number of resolvable modes for their method by finding the deviation of the reconstructed eigenspectrum from the 'True' spectrum. Because the V-K method is independent of initial guess it provides the maximum number of resolvable modes [15]. Figure 14 shows and example of V-K convergence with the optimum number of modes being 15. Deviation from the 'True'

spectrum is not robustly defined by the V-K method. Because the optimum reconstruction should contain the lowest error, the optimum mode for the V-K method was found by determining the field with the lowest L_2 error. The spectrum from the 12^{th} mode of reconstruction does diverge before the 15^{th} mode is reached but is a consequence of only use 12 modes in the reconstruction.

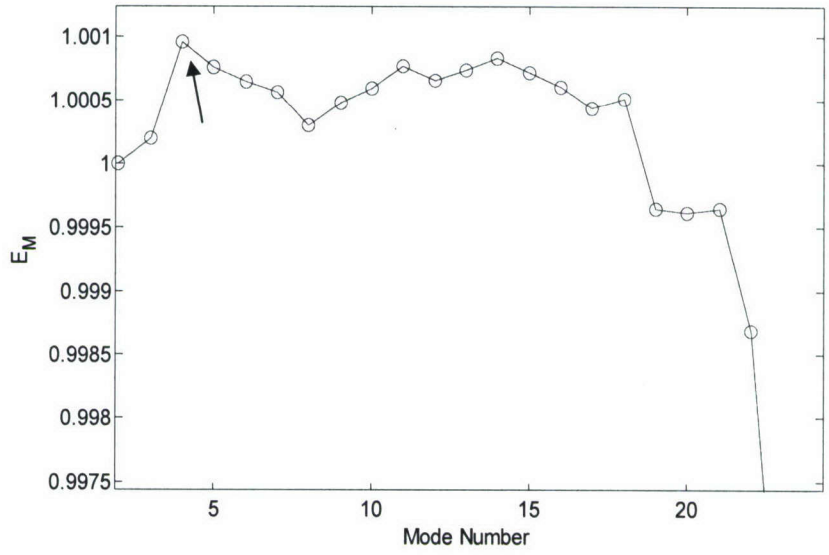


Figure 13. Convergence for E-S method determined by equation 9. The arrow denotes the maximum mode number.

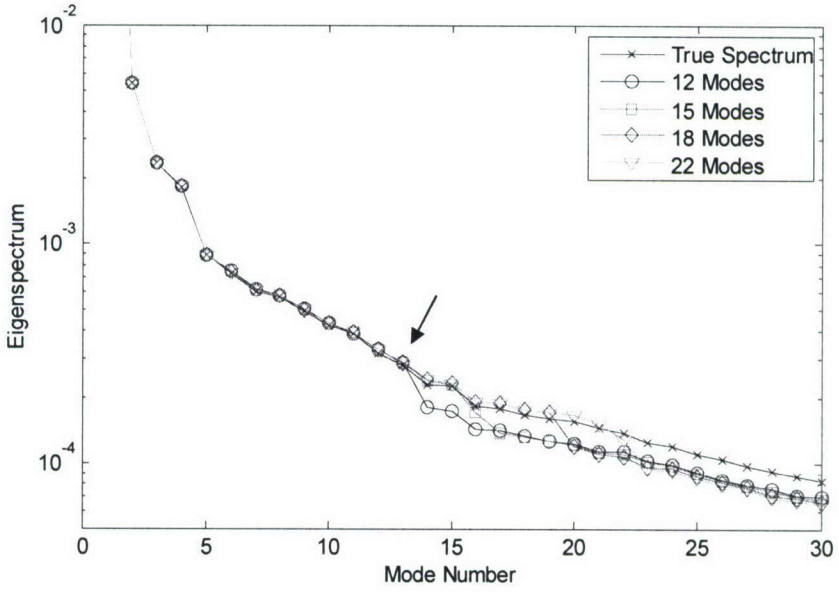


Figure 14. Demonstration of the V-K convergence method or 11% 3x3 gappy DNS data. The arrow locates the deviation from the 'True' spectrum.

Using experimental data, this 'True' spectrum will not be known and therefore cannot be used in determining convergence. It is possible to generate a 'True' eigenspectra from DNS but a complete DNS solution must be computed accurately to represent the exact data set [21]. A robust definition for deviation is also required for this method in order to be applicable.

3.D.III CONTINUITY BASED CONVERGENCE CRITERIA (CBCC)

Fields commonly encountered in planar PIV as well as MRV are nearly 2-D in nature and should obey the continuity equation. These experimental 2-D fields will not be divergence free because experimental error and stray vectors will in turn cause derivative values to contain a certain amount of error. These factors should be consistent and therefore should be independent of any gaps in the field. The formulation of the continuity equation in a 2-D incompressible flow is:

$$R = \frac{\partial u}{\partial x} + \frac{\partial v}{\partial y} \tag{11}$$

where u and v are the Cartesian velocity components in the x and y directions respectively. R is the residual produced by experimental error stray vectors and the missing out-of-plane velocity gradients.

This equation is applied after each mode is converged in the V-K method (in between steps a) and b)). Gaps in the data will produce large discontinuities in the velocity field which will lead to high localized velocity gradients and residuals. Through minimization of this residual over the entire field the optimum number of modes to use in the V-K method of reconstruction is determined. Figure 15 shows a plot of the residual values

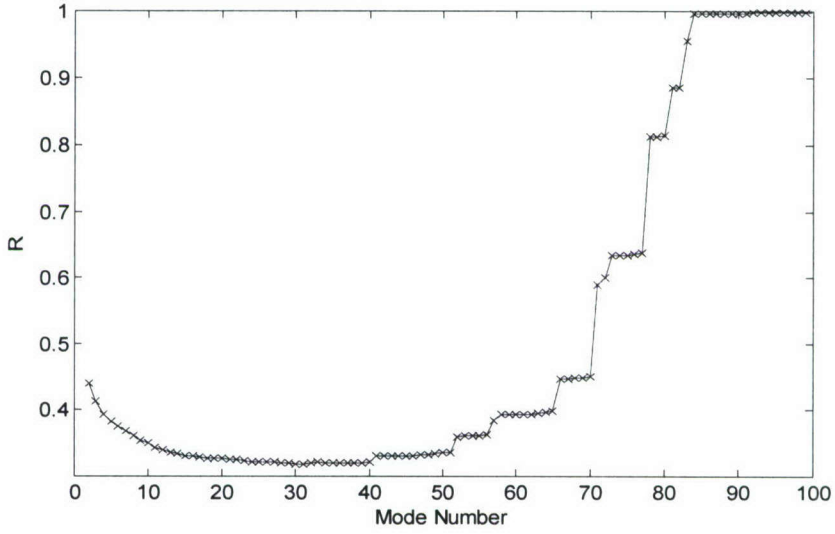


Figure 15. Convergence criteria for the V-K method using a reduced form of the continuity equation. The arrow indicated the minimum residual from equation 31.

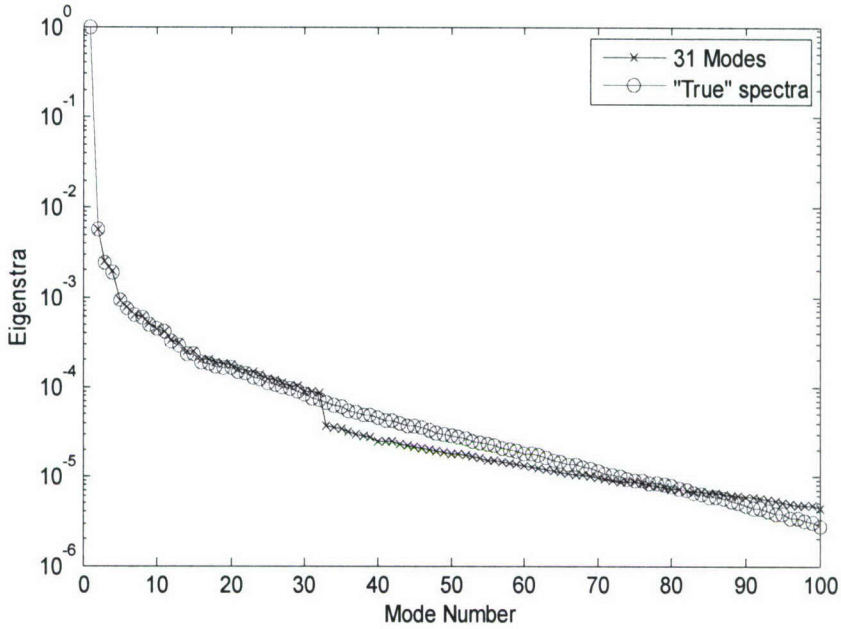


Figure 16. Eigenspectra for the corresponding converged minimum from Figure 15. The 'True' solution is shown to help illistrate divergence.

as the mode number is increased using the V-K Method. All of the residual values have been normalized against their individual maximum value for easier comparison between cases. While the mode number found from the continuity equation does not exactly match that of the V-K method it will be shown that the error is within experimental uncertainty and is maximally resolved. Figure 16 shows the eigenspectra from the converged result plotted against the 'true' solution. The errors associated with this new convergence criteria will be discussed in the next section.

3.E. RESULTS

3.E.I GAPPY PERCENTAGE AND SIZE RESULTS

In order to robustly test the applicability of the CBCC, a wide range of gappy fields where tested. As mentioned, fields with 5%, 11%, 20%, 50%, and 80% gappyness were produced with gap sizes of 1x1, 3x3, 5x5, and NxM. Grid size NxM was tested to help simulate experimental data.

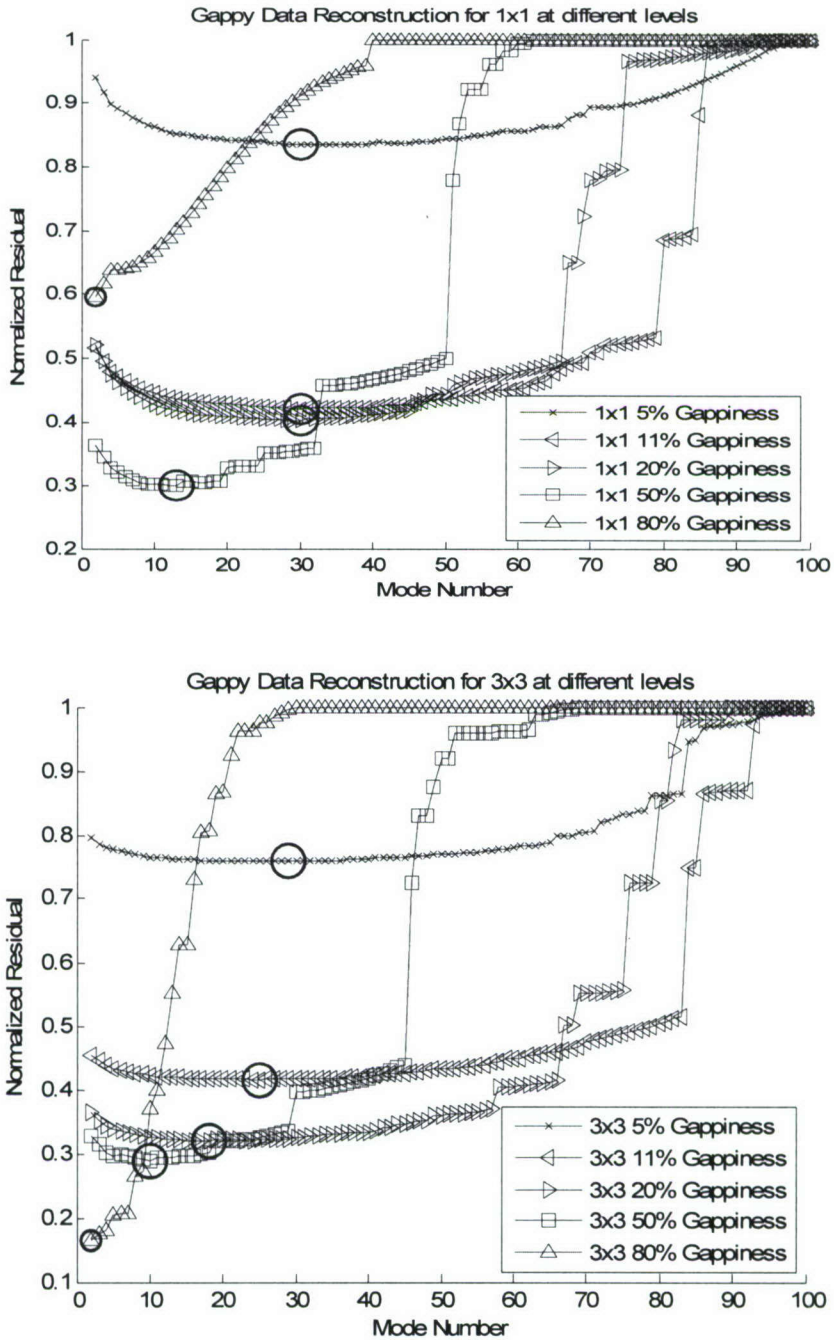


Figure 17. Residual determined from the CBCC with gappyness spacing's of a) 1x1, b) 3x3, c) 5x5 and d) NxM. All Residual values are normalized with their maximum value to produce a range of 0-1. The Circles indicate the minimum for each gappyness level.

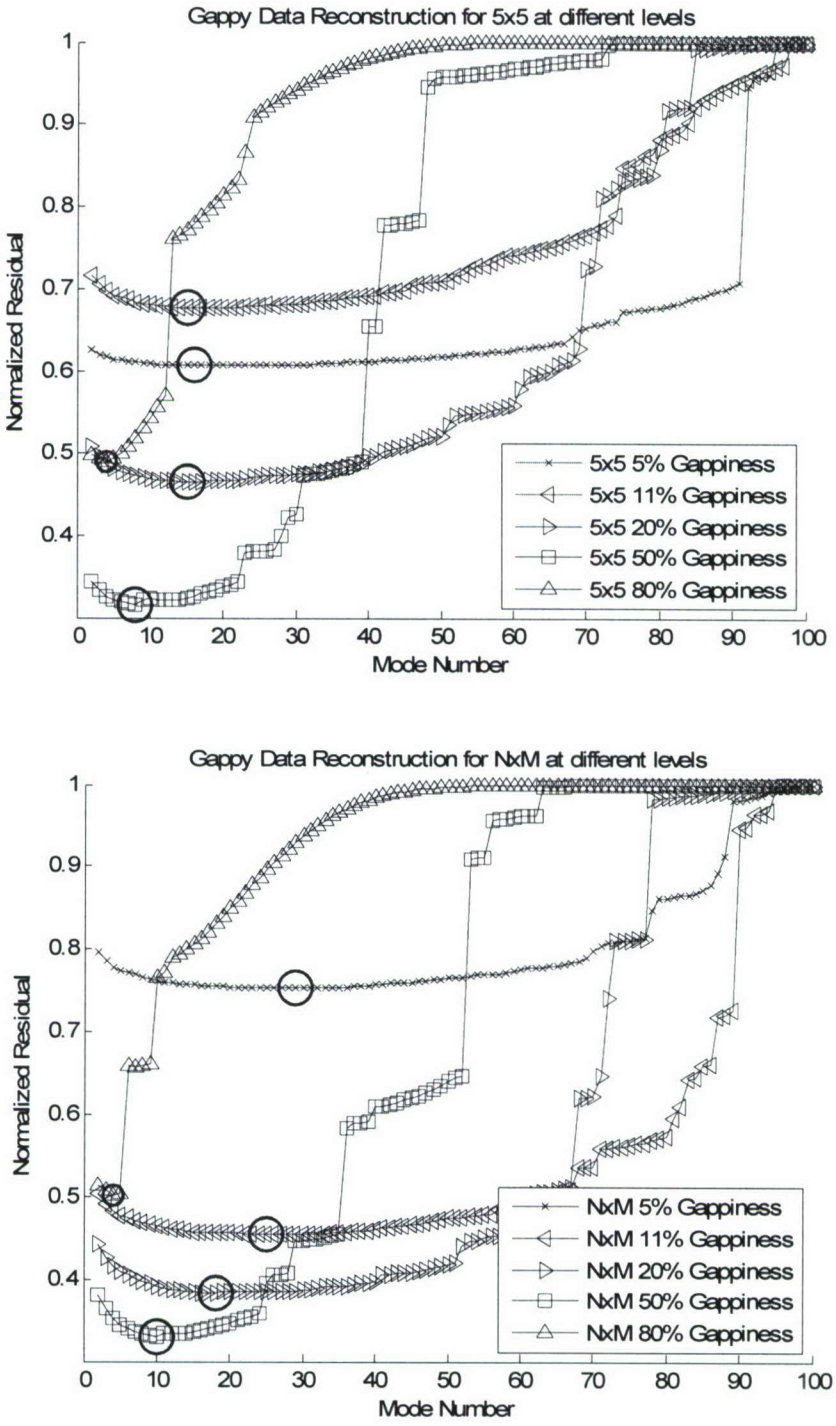


Figure17. Continued. Residual determined from the CBCC with gappyness spacing's of a) 1x1, b) 3x3, c) 5x5 and d) NxM. All Residual values are normalized with their maximum value to produce a range of 0-1. The Circles indicate the minimum for each gappyness level.

As mentioned, by minimizing the residual from the two dimensional continuity equation the maximum number of experimental reconstruction modes can be found. From Figure 17, it can be seen that the minimum residual value falls within the first 40 modes for 5% to 50% gappyness. The 80% gappyness case does not demonstrate a true minimum and as a result will not to work with this criterion. Eighty percent gappy is a very difficult case as only 20% of all possible points are in fact good measurements. With a lower total number of bad points it can be understood that a higher number of resolvable modes would be found. This is because the discontinuities in space and time are less frequent for larger gappyness cases. The number of resolvable modes decreases slightly, also when the grid spacing increases. This is attributed to the increased spread of bad information to the surrounding points during the reconstruction. For the NxM case the number of resolvable modes is the same as the 3x3. This is understandable as the mean value of the NxM block sizes is 3x3. This shows that limitations on reconstruction will be gappyness percentage and average grid size with gap uniformity of having less of an effect.

Figure 18 shows the different eigenspetra plotted against the 'true' solution as done by Venturi and Karniadakis [15]. It can be seen that the eigenspetra stay attached until they reach the CBCC optimum mode of reconstruction. The deviation seen at the CBCC determined mode is different than the deviation discussed by Venturi and Karniadakis. This divergence is due solely to the fact that only a selected number of modes was used in reconstruction and there a deviation will be seen at that particular mode number. These CBCC determined modes can reconstruct the flow with errors on the other or below experimental error. These errors will be discussed in the next section.

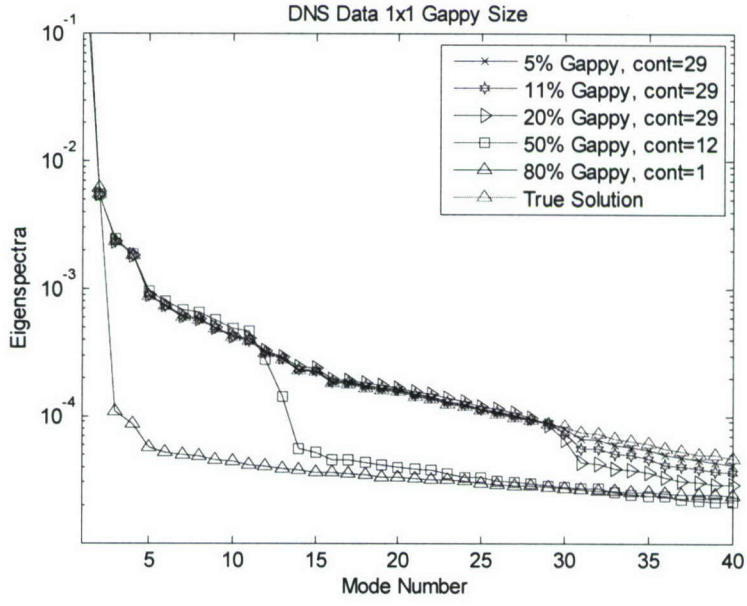


Figure18. Eigenspectrums from the CBCC determined optimum modes of reconstruction with different gappyness spacing's a) 1x1, b) 3x3, c) 5x5, d) NxM.

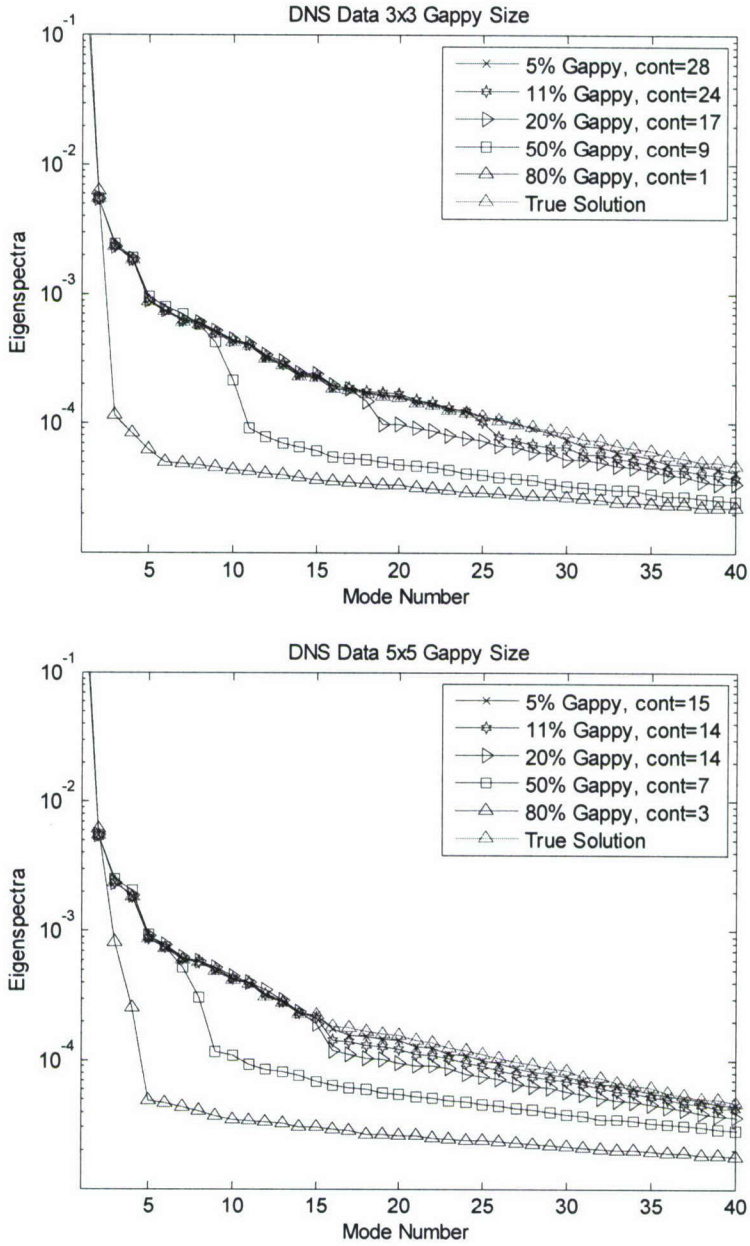


Figure 18. Continued. Eigenspectrums from the CBCC determined optimum modes of reconstruction with different gappyness spacing's a) 1x1, b) 3x3, c) 5x5, d) NxM.

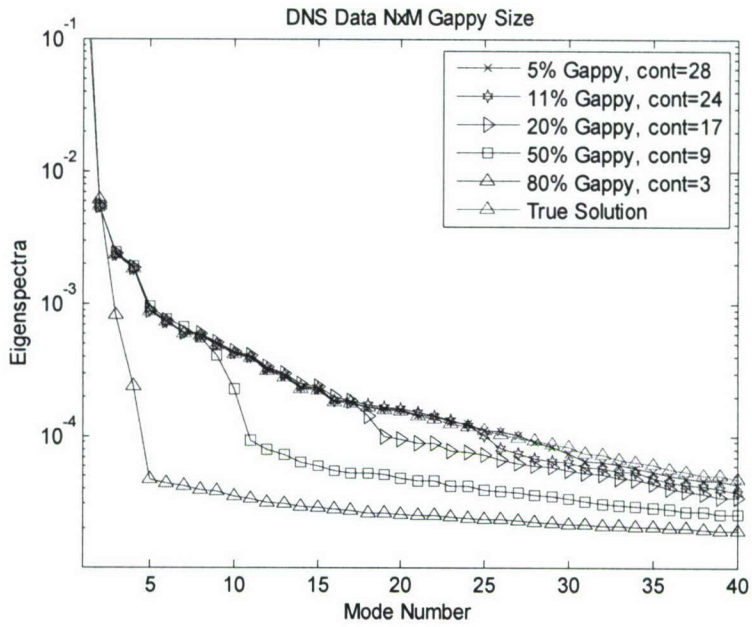


Figure18. Continued. Eigenspectrums from the CBCC determined optimum modes of reconstruction with different gappyness spacing's a) 1x1, b) 3x3, c) 5x5, d) NxM.

3.E.II FIELD ERROR ANALYSIS

When evaluating the errors due to reconstruction two reconstruction fields were used. The first field was the reconstructed field determined by the CBCC as mentioned before. The second was the field that contained the lowest L_2 error. The lowest L_2 error was found by comparing each reconstructed field to the true solution. The optimum reconstructed field would be by definition the field with the lowest error when compared to the true solution. Errors were calculated using equations 12 and 13. These values were normalized by the velocity magnitude of the field in order to produce a percent error. Using these two fields will help to determine how close CBCC gets to a true optimal reconstruction.

$$L_2\ Error = \frac{\left\| Ur\left(M=0\right) - UT\left(M=0\right)\right\|_2}{\left\| \sqrt{U_T^2 + V_T^2} \right\|_2} \tag{12}$$

$$Max\ Error = \left\| U_r^2\left(M=0\right) - U_T^2\left(M=0\right)\right\|_\infty \tag{13}$$

Figure 19 shows a side by side comparison of error values found from the CBCC and the true optimum field. These values are seen to be comparable both in L_2 error and maximum error. The 5x5 gappy spaced fields do show large values in both L_2 error as

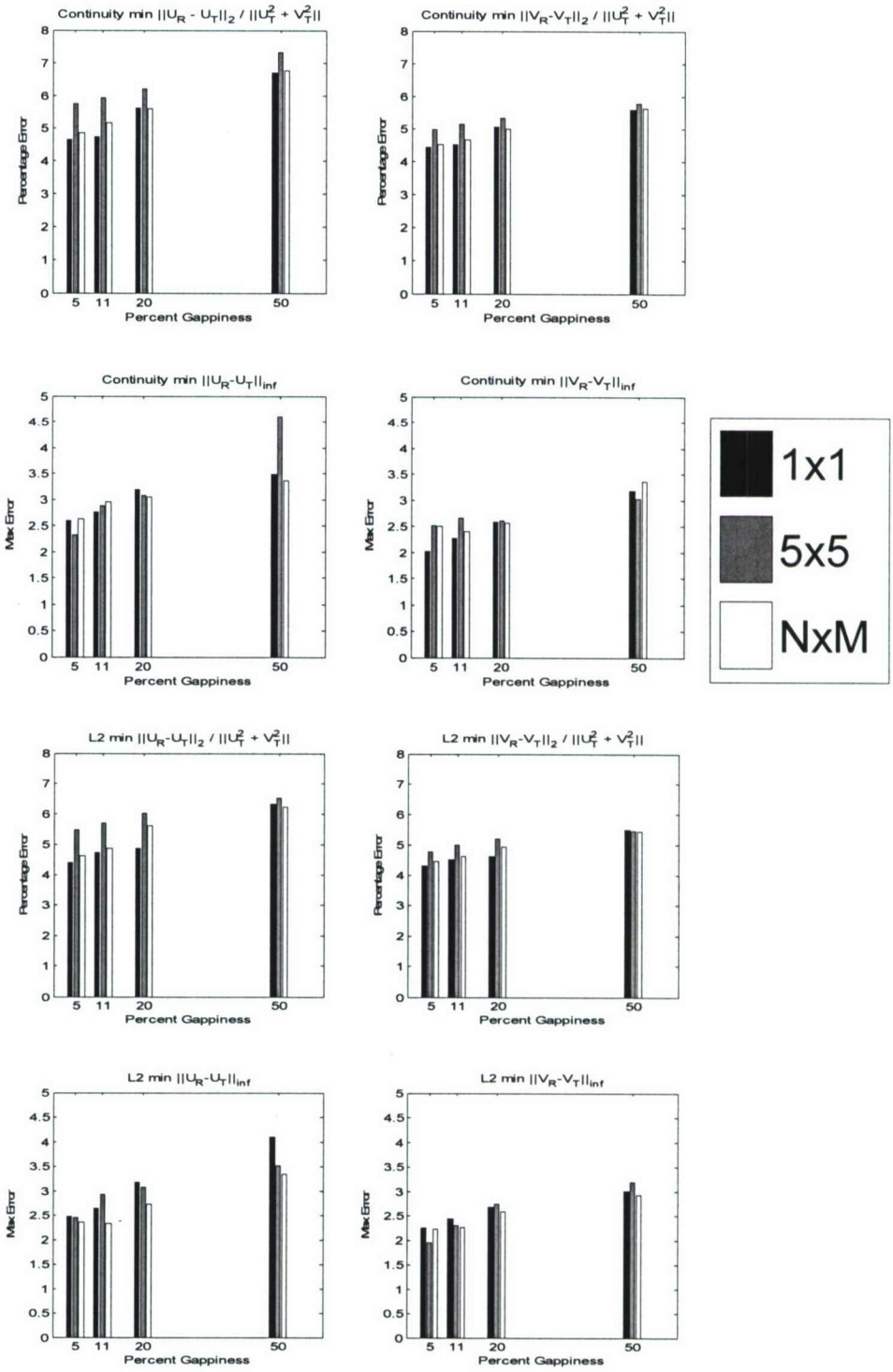


Figure 19. Error comparison for the CBCC determined optimum construction compared to the field containing the lowest L_2 error. The bar colors from dark to light represent 1x1 to NxM respectively.

well as maximum point wise error. Figure 20 shows the difference between these two fields. With less than one percent difference between the two fields this is below experimental error commonly found with PIV and MRV images. This demonstrates that while the CBCC may not find the true optimum mode it can be trusted within experimental error.

3.F CONCLUSIONS

This work has demonstrated an experimental convergence criteria for the method set forth by Venturi and Karniadakis for gappy data reconstruction using Proper Orthogonal Decomposition. Through the minimization of the residual produced by the two dimensional version of the continuity equation the optimal reconstruction mode number can be determined. As shown by Venturi and Karniadakis, their iterative procedure for data reconstruction produced higher accuracy results as compared to linear interpolation as well as other POD based reconstruction methods. Providing a convergence criterion now makes the method applicable to those in experimental fields wishing to reconstruct gappy or incomplete measurements.

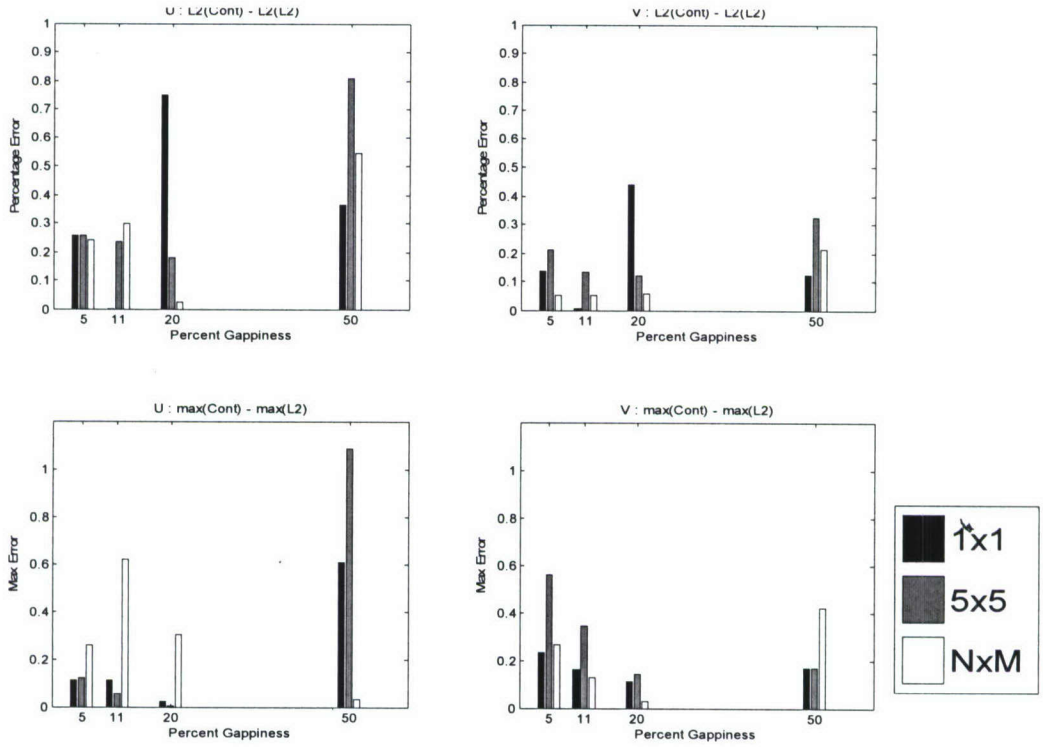


Figure 20. Error Differences between the CBCC reconstruction and the reconstruction with the lowest L2 error.

4. WALL JET

In order to demonstrate the capability of making high speed TR-DPIV measurements in a transonic cascade a bench top experiment of a turbulence wall jet was undertaken. This experiment provided high sampling frequency (kHz rate) high speed and high magnification velocity measurements.

4.A. INTRODUCTION

A wall jet is created when a fluid moving over a wall exceeds the velocity of the free stream. The applications for these jets are wide ranging and are commonly seen in heating and cooling applications such as gas turbine blade cooling [22, 23]. These jets are typically broken down into three distinct regimes: near wall boundary layer, mixing layer, and outer shear layer [24].

While shear flows have been studied extensively both spatially and temporally [25, 26], wall jets have not been investigated to this degree. Strong anisotropic characteristics of the flow and the coexistence of multiple length scales and extreme velocity gradients have made conventional experimental methods inadequate for resolving such flows. While previous studies typically allow for either spatial or temporal resolution, this study investigates the transitional wall jet with high spatial and temporal resolution.

Previous studies, have provided a great deal of information on the basic development of these jets, including that of Launder and Rodi who published an inclusive summary of work done before 1981 [22]. Chun and Schwarz and showed the critical Reynolds number of wall jets to be 57 [27]. With this knowledge, we may assume that for many engineering applications almost all wall jets will either be transitional or fully turbulent. While wall jets within transitional Reynolds numbers impose more challenges to analyze, fully developed turbulent wall jets have been shown to be self-similar allowing for scaling parameters to be applied across a large range of Reynolds numbers[28, 29]. An empirical formulation of the downstream profile of a fully developed jet was set forth by Schneider but this study was limited in Reynolds number and focused only on far downstream locations, avoiding the developmental region [29].

While research was been done on full developed wall jets only a limited amount it know about the transition to turbulence. Bajura and Catalano have shown that the transition process for wall jets contains multiple stages which rely heavily on vortex formation and coalescences between the inner and outer regions of the jet [30]. This information is limited to the downstream locations as the authors only study lateral positions of X/H = 18 – 180 (lateral distance over jet slot height).

Additionally, the works by Gogineni et al. and Gogineni and Shih investigated transitional wall jets both numerically as well as through the use of PIV [31 ,32]. These works helped showing the impact of vortex formation inside as well as outside of the outer shear layer. Although this study was limited to one Reynolds number, results

clearly showed vortex pairing across the shear layer which led to break up and turbulent transition of the jet [31].

Proper Orthogonal Decomposition (POD) has been widely used in dynamical systems modeling and in the analysis of turbulent flows. POD is a mathematical tool that generates a low dimensional representation of high order systems [33,34]. Reducing highly spatially and temporally resolved complex flow fields in this way can be very beneficial for developing an understanding of the underling physics. It has been used to study both near wall and turbulence shear environments with great success [35, 36].

In this study, wall jets with Reynolds numbers from 150-10,000 were studied. Through the use of POD in combination with vortex identification schemes, the dynamics of developing transitional wall jets were investigated.

4.B. NOMENCLATURE

$U(\vec{x})$ Single Velocity field, (x,y) at a single time step.

$\phi(\vec{x})$ POD eigenfunction determined using Karhunen- Loéve Decomposition.

λ Eigenvalue produced from Karhunen - Loéve Decomposition.

$\phi^{(s)}$ POD eigenfunction determined using method of snapshots.

$\alpha^{(s)}$ Projection coefficient associated with the method of snapshots.

$\langle \cdot \rangle_t$ Ensemble average over time.

H Wall jet slot height.

U_0 Jet exit velocity.

$y_{1/2}$ Vertical position for which $U(x) = U_0/2$ at a given x

S, Ω Symmetric and anti-symmetric velocity gradient tensor, respectively.

$\det(\cdot)$ Determinate of a matrix.

$\lambda_{1,2,3}$ Eigenvalues from the λ_2 vortex identification scheme.

4.C. EXPERIMENTAL SETUP

This experiment was conducted using a jet with a slot height of 2 mm and an aspect ratio of 18.5:1 (jet width / height). A total of nine different Reynolds numbers were tested ranging from 150 – 10,000. The Reynolds numbers were based on the slot height and nozzle exit velocity. Table 3 shows each Reynolds number and corresponding exit velocity. The mid-spanwise plane of the jet was investigated, focusing on a 4 mm x 20 mm field of view (2H x 10H). Figure 21 shows a schematic of the test setup.

Table 3. Experimental Parameters.

Reynolds Number	Jet Exit Velocity	Sampling Rate	Pulse Separation
150	1.10 m/s	1000 Hz	65 μs
200	1.49 m/s	1000 Hz	47 μs
750	5.63 m/s	1000 Hz	12 μs
1,000	7.51 m/s	1000 Hz	9 μs
1,500	11.25 m/s	1000 Hz	6 μs
2,000	14.95 m/s	2000 Hz	5 μs
5,000	37.47 m/s	2000 Hz	2 μs
7,500	56.20 m/s	2000 Hz	1 μs
10,000	75.44 m/s	2000 Hz	0.92 μs

All measurements in this study were preformed with Time Resolved Digital Particle Image Velocimetry (TR-DPIV) using a kHz Nd:YAG dual head laser. The use of a dual head laser allows for a reduction in the laser pulse separation to values as low as 50 ns. This capability is imperative to allow for high magnification measurements to be taken at high speeds. An IDT XS-5 CMOS digital camera with kHz sampling was utilized for data collection. To achieve the required sampling rate, the resolution was set to 256x1280 for all cases. The flow fields for the lower Reynolds numbers (Re=150 – Re=1500) were sampled at 1 kHz while cases for higher Reynolds numbers (Re=2000 - Re=10000) were sampled at 2 kHz. Pulse separations were calculated depending on

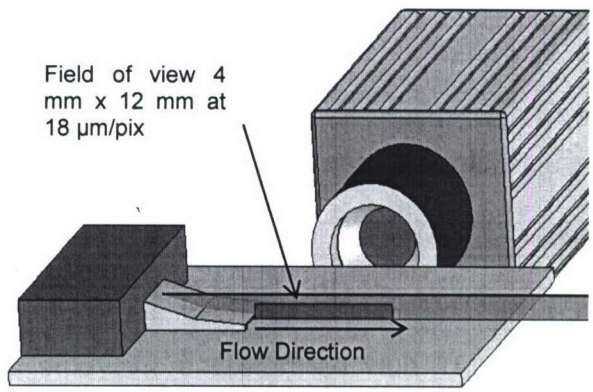


Figure 21. Experimental Setup. The red box represents the field of view of the camera while the green line is the laser plane entering from the right.

the flow speed and the ¼ rule imposed by the DPIV optimum interrogation window size and were found to be between 50 μs - 900 ns for the Reynolds numbers stated above. Seeding was generated using a Laskin nozzle with Diethylhexel sebacate (DHS). The estimated seeding density was 20 particles per 32 pixel window with an approximate droplet size was 1.0μm. Considering the fluid properties, we estimated that the Stokes number was on the order of $1x10^{-5}$ to $1x10^{-3}$ for velocity ranges of 1 – 75 m/s. Figure 22 shows and instantaneous images from a Re = 750. Seeding in the flow above the shear layer was not possible due to its quiescent nature.

All TRDPIV images were processed using an in-house PIV code and utilized a Robust Phase Correlation (RPC) technique [9] coupled with a second-order discrete window offset technique [37]. The RPC method provided higher accuracy over standard cross correlation techniques by using dynamic phase-only filters along with an a priori spectral energy filter. It also has the advantage of greatly reducing peak-locking effects versus standard cross-correlation techniques. The resulting fields were validated by a median filter for each point using 5x5 surrounding points. Bad vectors where replaced using a weighted linear interpolation. Once vector fields were estimated, the data was post-processed using standard analysis tools such as statical analysis of first and second order moments of the velocity field, vorticity estimation, spectra etc. In addition Proper Orthogonal Decomposition as described in following sections was implemented in order to help us reveal the underlying dynamics of the flow.

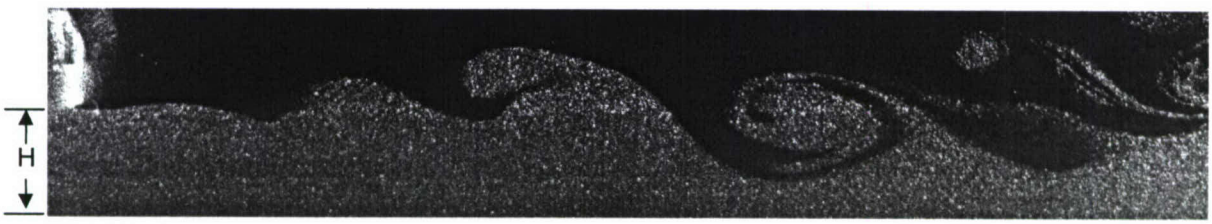


Figure 22. Example instantiations image for Re 750. Here larger structures are seen to develop within

4.D. PROPER ORTHOGNAL DECOMPOSITION

For completeness, a short review of Proper Orthogonal Decomposition is included below, for more information please see [38 - 40]. The basic formulation of POD starts with the Fredhom Equation (2).

$$\int \left\langle U\left(\vec{x}\right) \otimes U\left(\vec{x}'\right) \right\rangle \phi\left(\vec{x}'\right) d\vec{x}' = \lambda \phi\left(\vec{x}\right) \qquad (14)$$

To apply POD to discrete velocimetry data, the equation must be discretized, by methods shown in equation (3). Here, $C_{i,j}$ is the two point correlation tensor which is ensemble averaged over the total number of frames or snapshots as described in equation (4).

$$\sum_p \sum_q C_{i,j}(x,y;p,q)\phi_j^{(s)}(p,q) = \lambda\phi(x,y) \tag{15}$$

$$C_{i,j} = \left\langle U_i(x,y;t)U_j(x,y;t)\right\rangle_t \tag{16}$$

To minimize computational time, the method of snapshots is used [34]. This method assumes that the eigenfunctions created with equation (3) are a linear combination of each the flow field snapshots multiplied by a corresponding projection coefficient.

$$\phi_j^{(s)}(x,y) = \sum_t \alpha^{(s)}(t)U_i(x,y;t) \tag{17}$$

By applying equation (5), to equation (3), the method of snapshots may be performed to obtain the reduced eigenvalue problem seen in equations (6) and (19).

$$\sum_n F_{n,l}\alpha^{(s)}(n) = \lambda^{(s)}\alpha^{(s)}(l) \tag{18}$$

$$F_{n,l} = \frac{1}{N}\sum_x \sum_y U_i(x,y;n)U_j(x,y;l) \tag{19}$$

Due to the orthogonality of the eigenfunctions, equation (5) can be rearranged to solve for the reconstructed flow field, where S is the number of modes used in reconstruction (equation8).

$$U_i(x,y;t) = \sum_t \alpha^{(s)}(t)\phi_j^{(s)}(x,y) \tag{20}$$

Therefore the fields are decomposed into temporal and spatial modes describing the energy and the structure of the flow respectively.

Equation (21) represents how the individual energy of each mode is determined, where λ_j is the eigenvalue associated with the j^{th} mode number. By ordering the modes and temporal coefficients based on their individual energy, the relative dominance of each mode can be determined as shown by equation (21). Because the current study is interested in the energy associated with each mode and its influence on turbulence transition, the modes are organized by energy contribution.

$$\text{Energy Fraction} = \frac{\lambda_j}{\sum_j \lambda_j} \tag{21}$$

In order to create a reduced model the number of modes used in reconstruction will be determined by calculating a cumulative sum of the eigenvalues with respect to the

total sum. This cumulative sum value will provide the percent energy included in a particular model. For the present study, all of the Reynolds numbers were reconstructed so that 99% of the total energy was captured. Figure 23 shows a plot of cumulative energy with respect to mode number. What is important to note is the amount of energy contained in the first mode. The first mode strongly resembles the time averaged profile as they will be the most predominate features of the flow. Table 4 shows the number of modes required for each Reynolds number to meet the 99% energy criterion with and without the use of the first mode.

Table 4. Number of modes required to reconstruct 99% of the cumulative energy w/ and w/o the 1st Mode.

Reynolds Number	# of Modes Containing 99% of the Total Energy	# of Modes Containing 99% Total Energy w/o 1st Mode
150	1	1366
200	1	1299
750	213	1254
1,000	158	1150
1,500	125	1107
2,000	729	1402
5,000	256	1349
7,500	378	1380
10,000	177	1338

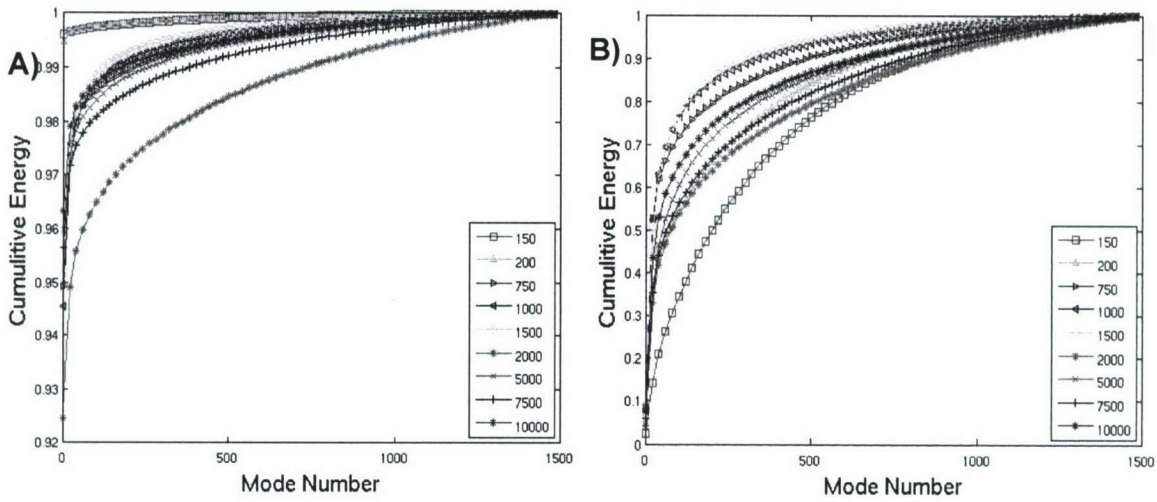


Figure 23. Cumulative energy from POD. A) Cumulative energy for All Modes. B) Cumulative excluding the 1st mode

4.E. VORTEX IDENTIFICATION

In order to determine the location of vortices in the developmental region of the jet, the λ_2 Vortex Identification Scheme (λ_2-VIS) was performed on the data reduced by POD

[41]. The criteria of λ_2-VIS states that a vortex can be identified by the use of equation (22),

$$\det\left(\left[S^2+\Omega^2\right]-\lambda \mathrm{I}\right)=0 \qquad (22)$$

where S and Ω are the symmetric and anti-symmetric parts of the velocity gradient tensor. A vortex is detected if λ_2, the second lowest eigenvalue when ordered by magnitude, is less than zero. This occurs when two positive eigenvalues of the local pressure Hessian exist. This method has been widely used and has shown to have advantages over many conventional local approach based methods [41].

Prior to applying λ_2-VIS, the data was reduced through POD, in order to capture 99% of the total energy with the first mode subtracted (column 3 of Table 4). The number of modes required to capture this energy was determined by equation (21). Removing the time average or convective component of the flow dramatically assists in identifying vortices among the different Reynolds numbers. Because this scheme is Galilean invariant it is acceptable to remove the convective component [41]. Figure 24 shows the λ_2-VIS applied to an instantaneous frame (A) and a reconstructed frame (B) from Re = 10,000.

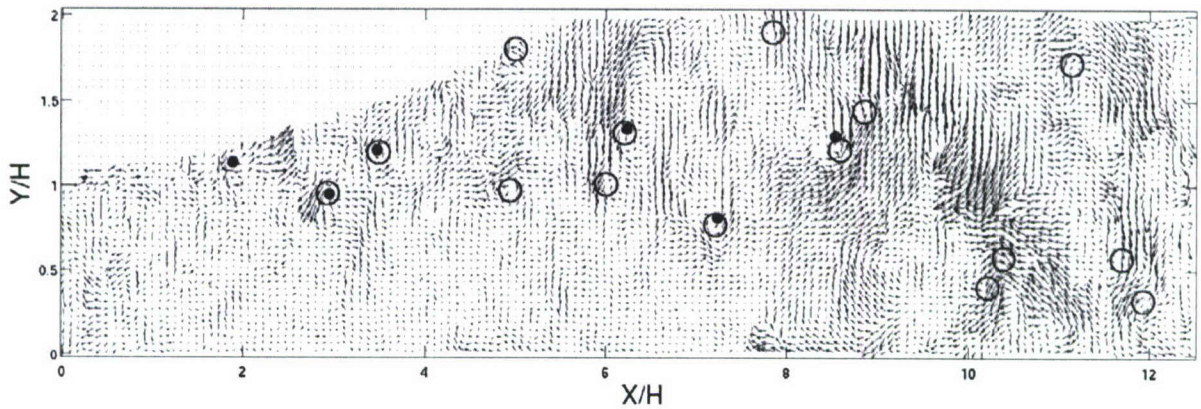


Figure 24. This figure shows the location of discrete vortices from Re = 10000. The close circles (•) represent vortices found using instantaneous flow field while the open circles (o) represent the vortices found using the POD reconstructed field

4.F. RESULTS AND DISCUSSION

4.F.I TIME AVERAGED ANALYSIS

In order to compare with previous works, the data was initially approached in a time-averaged manner. By non-dimensionalizing the velocity profiles with $y_{1/2}$ and the jet exit velocity with U_0, it can be seen that all profiles collapse to a single curve. Figure 25

shows these velocity profiles at several downstream locations. These plots strongly resemble previous findings for similar experiments [22, 28, 29, 31, 42]. In part D) of Figure 24 an empirical curve presented by Schneider is shown along with the time averaged velocity profiles of X/H = 10 [29]. Because Schneider's work focused with develop further downstream of the jet exit good agreement is only seen with the last location of this study. A numerical study by Levin et al. did investigate flow closer to the jet [43] in which the reported velocity profiles strongly resemble those of this study.

Figure 25 shows all of the Reynolds number of this study except of the lowest two (Re = 150 and 200). At this low of a Reynolds number the jet develops much more slowly and requiring more than 12H before they demonstrate a self similar profile. Although time-

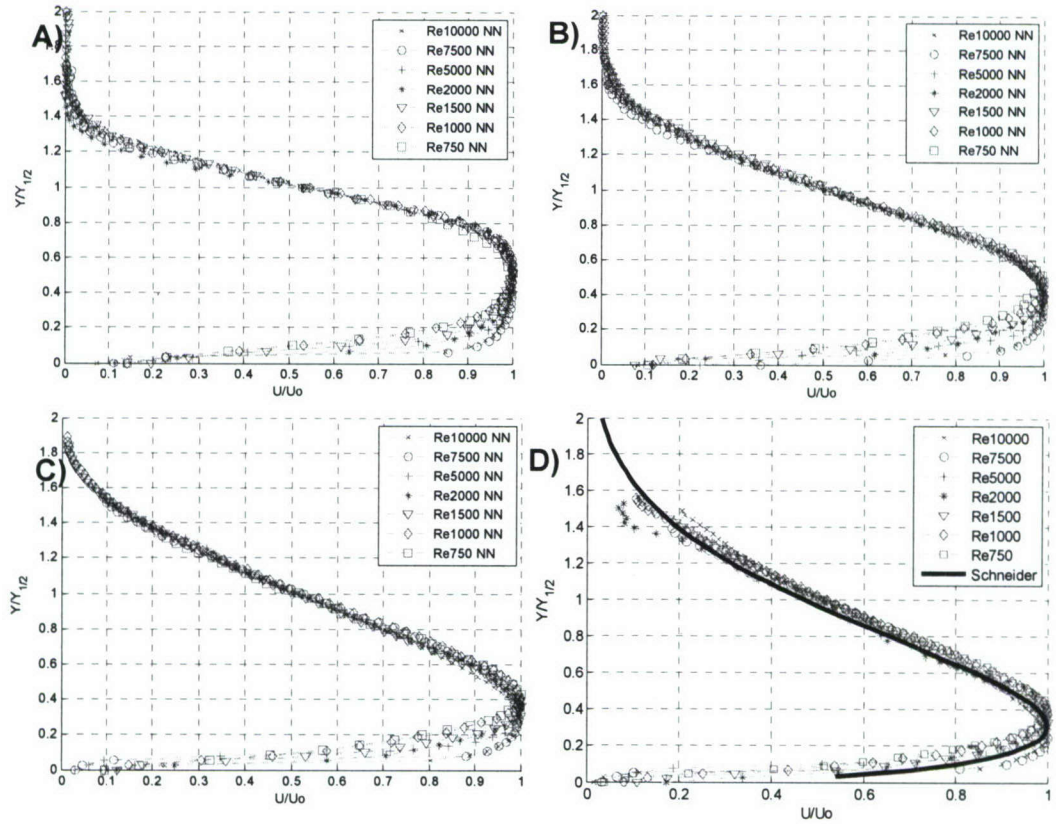


Figure 25. Time average velocity profiles for different Reynolds numbers at different X/H locations: A) X/H=3, B) X/H = 5, C) X/H = 7, D) X/H = 10. Figure D) also shows and empirically derived self similar profile for the jet.

averaged evaluations of wall jets are not the primary aim of this study, strong agreement with velocity profiles verifies that the experiment was successful in capturing the true physics of the flow.

4.F.II PROPER ORTHOGONAL DECOMPOSITION:

Spatial Analysis: Reducing data by means of POD is beneficial for several reasons. First, Proper Orthogonal Decomposition allows for a low order model to be produced. These lower ordered models most frequently contain reduced levels of noise. Secondly, POD decouples the spatial and temporal information. This decoupling allows for the independent investigation of spatial or temporal dynamics without influence from its counterpart. Figure 26 shows 3 spatial modes and their corresponding projection coefficients for a Re = 750. In this section the spatial structure of the flow field is presented.

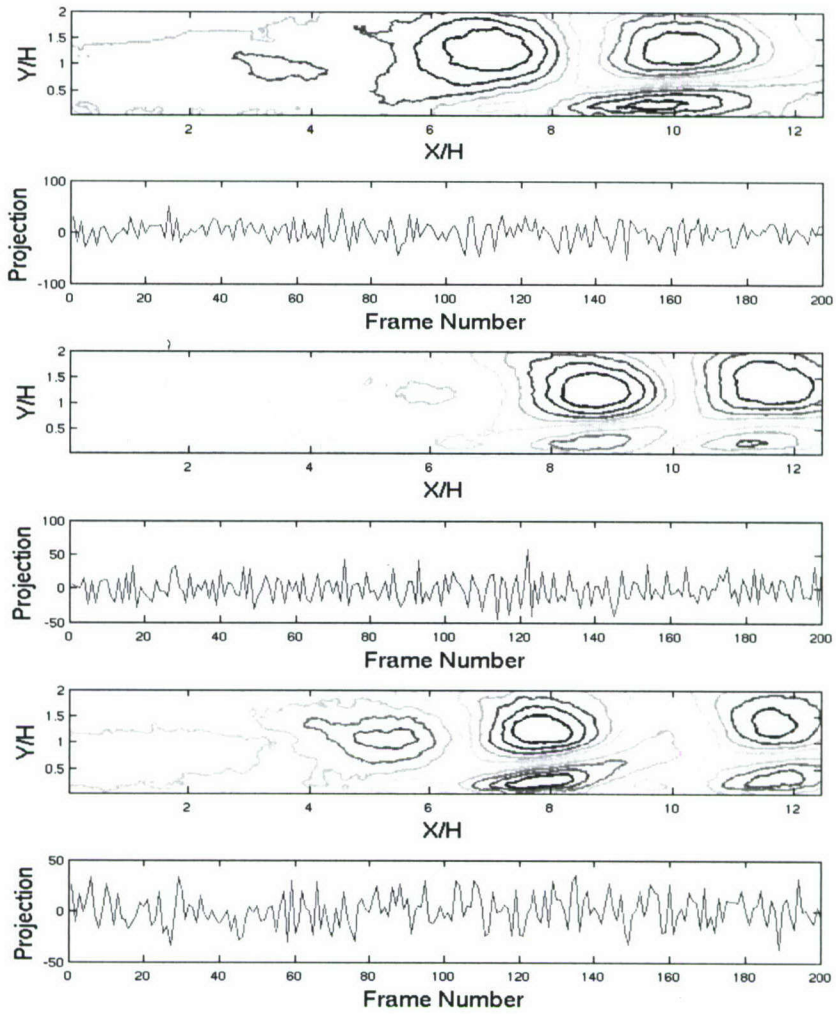


Figure 26. Contour Plots of the Stream wise POD modes and their corresponding projection coefficients for Re = 750: A) Mode 2. B) Mode 3. C) Mode 4.

As seen from equation (20), all of the spatial information is contained in the eigenfunctions, $\phi^{(s)}$, also referred to as the spatial modes. These spatial modes have dimensions of x, y, and mode number. As mentioned above, this study orders the POD modes based on their individual energy. When this is done, the first mode in all cases is nearly identical to the time averaged flow field therefore it is the most dominant. As a

the spatial modes is contained in the temporal coefficient, $\alpha^{(s)}$, and therefore should not be considered when analyzing these plots.

Temporal Analysis: For preliminary investigation of the temporal information gained from POD, a Power Spectral Density (PSD) analysis was performed on each temporal coefficient. Because the temporal coefficients have been decoupled from the spatial information, they provide a unique look at the frequency information contained inside these flow fields. By observing the power spectrum for each of the temporal modes, dominant frequencies of each of the modes may be determined. Additionally, an evaluation of the relative power of each of the modes provides the dominance of each of the different modes.

Because the spatial and temporal modes have been reordered based on energy, it is understandable that the most dominant frequencies would be found in the lower numbered modes (higher energy modes). Figure 28 shows a contour plot of the frequency information with respect to mode number for a Reynolds number of 200, 1000 and 10000. The contour values shown have been normalized with respect to the power from the dominant frequency for each Reynolds number. For lower Reynolds number cases, spectral energy is contained in the lower frequencies and spreads to

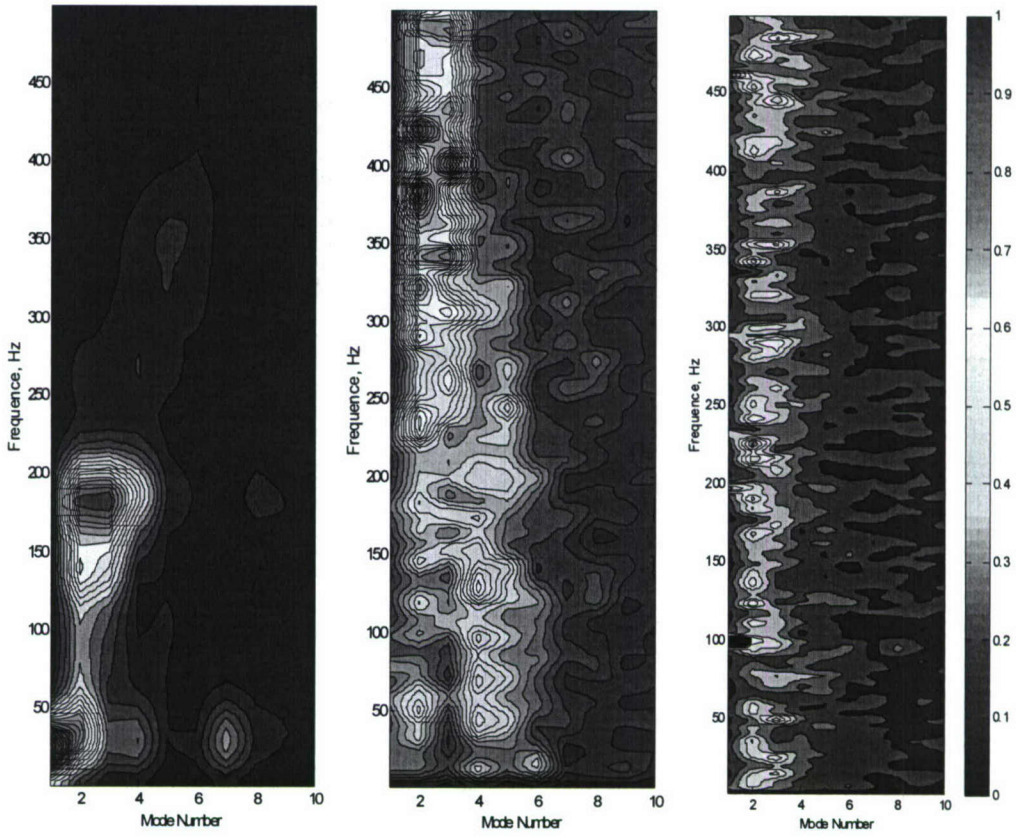


Figure 28. Contour plots of spectral density for the temporal coefficients of Re= A) 200, B) 1000, C) 10000. The contour shows power for each individual frequency normalized against the maximum value for each Revnolds number.

high frequencies as Reynolds number increases. It can be seen that the lower-numbered modes contain the most dominant frequencies and in fact mode numbers above 30 provide only a small contribution.

In an effort to consolidate the obtained data, Figure 29 shows a contour plot of dominant frequencies for each mode while the absolute maximum frequencies for each Reynolds number is listed in Table 5. Figure 29 helps to demonstrate that in addition to individual modal frequencies, the number of modes carrying high frequency information also increases with increased Reynolds number.

Table 5. Dominant Temporal mode with corresponding frequency for all 9 Reynolds numbers

Reynolds Number	Dominant Frequency	Mode Number
150	25	2
200	24	1
750	369	2
1000	421	2
1500	321	2
2000	380	2
5000	618	2
7500	221	1
10000	196	1

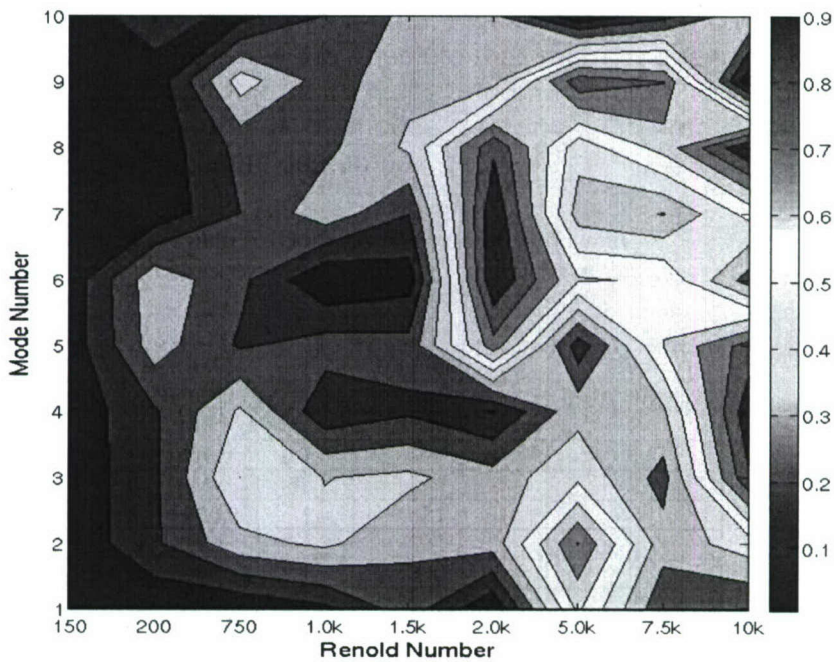


Figure 29. Contour plot of maximum frequency at each mode versus Reynolds 150 - 10000. The contour values have been normalized with 1kHz provide values from 0 -1.

It can be seen from Figure 29 that a dramatic rise in modal frequency occurs as the Reynolds number transitions from 1500 to 2000. This is also interesting in that two of the three modes with increased frequency have shown to be Reynolds number independent, based on our spatial analysis. This helps to illustrate the importance of using POD because while spatial information in the lower modes does not appear to very significantly differences in the temporal modes differ greatly.

4.F.III VORTEX IDENTIFICATION ON POD REDUCED FIELDS

Figure 30 shows a portion of the vortices located by the λ_2-VIS for four different Reynolds numbers: 150, 750, 2000 and 10000. It is interesting to note that for lower Reynolds number cases the majority of the vortices populate the region near the wall and the outer shear layer. As the Reynolds number increases, this behavior reverses

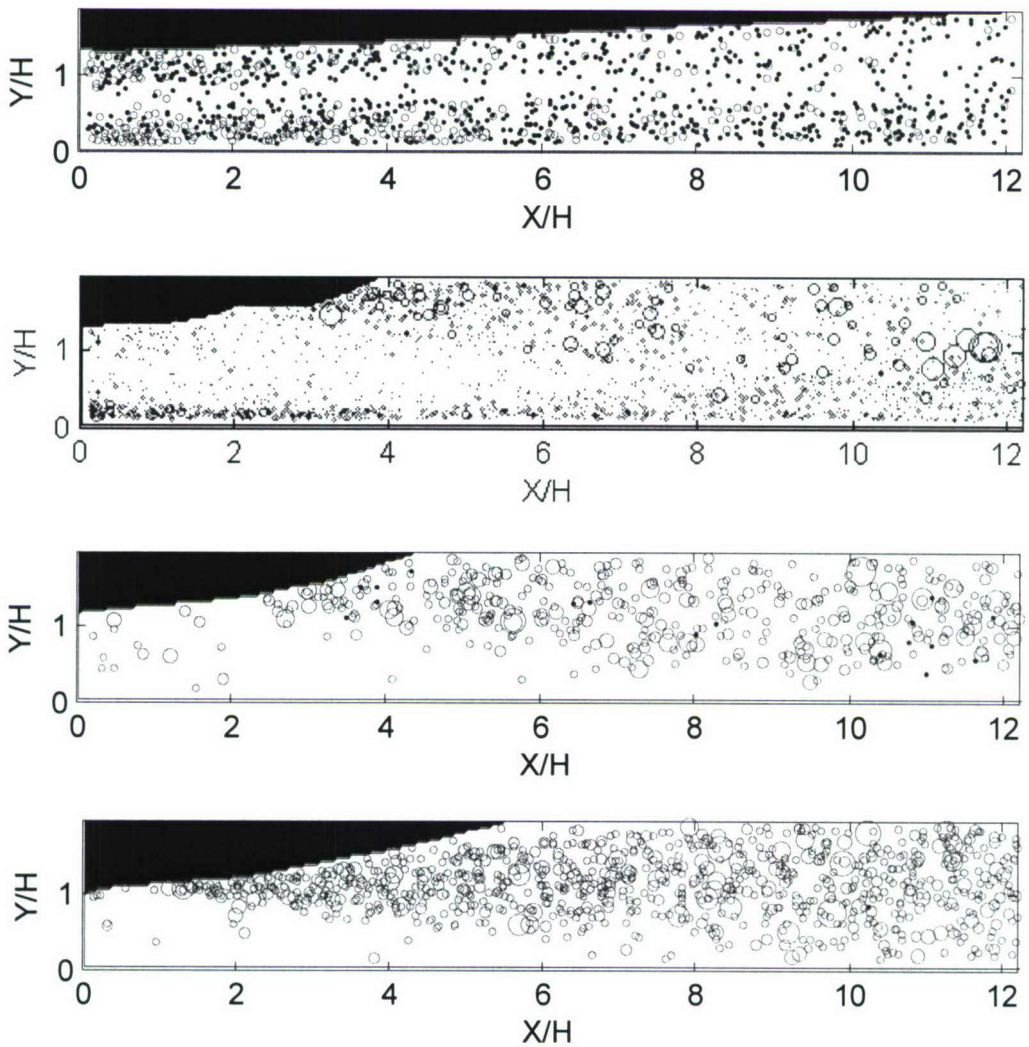


Figure 30. Vortex locations for 4 different Reynolds numbers: a) 150, b) 750, c) 2000, d) 10000

and although the vortices present in the flow increase in numbers they now move away from the wall into the mixing layer. This migration helps to show the dominance of fluctuation in the shear layer over the near wall region.

By plotting histograms of the vertical and horizontal location of the vortices, a better representation of the distribution can be seen. A surface plot of the distributions can be seen in Figure 31. This figure helps to further support the observation that the vortices appear to move away from the wall at the exit of jet and coalesce in the mixing layer. This coalescence occurs in the same vertical location as the stagnation point located in the first unsteady spatial mode. It should be noted that a step was located at the top of the jet exit as opposed to a fine edge. Having a step at the exit of the jet will create a recirculation region and is likely the reason for the vortices to appear around Y/H =1.

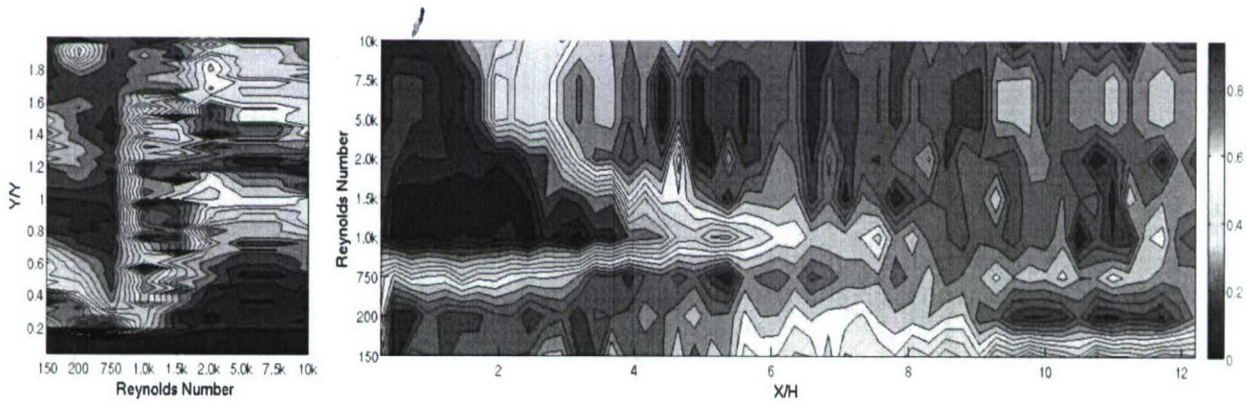


Figure 31. Surface plots of the vertical and horizontal histogram information. This plot shows that at lower Reynolds numbers vortices are seen close to the wall but as Reynolds number increase they move towards the shear layer.

4.G. CONCLUSION

Through the use of both TRDPIV measurements and POD analysis, a wall jet was studied through a wide range of Reynolds numbers. The time averaged data provided good agreement with previous data published in literature which helps to establish a basis for comparison. The spatial POD modes showed that some of the dominant structures in the wall jet appear to be independent of Reynolds number. This independence is seen through the first 5 unsteady spatial modes which include more than 99% of the total energy of the flow based on equation (21).

The temporal coefficients assist in the indication of the most dominant unsteady modes in the flow. An interesting discovery in this analysis was that some of the Reynolds number independent spatial modes begin to play an important role temporally in transition as the Reynolds number grows.

Through the use of vortex identification it was also possible to locate discrete vortices and to determine how the congregation coalesces of these vortices changed as Reynolds number was increased. The information obtained through this study aims to provide a better understanding of transitions to turbulence in wall jets.

5. HIGH SPEED CASCADE EXPERIMENT

This section will cover the demonstration of Time Resolved Digital Particle Image Velocimetry capability inside of the transonic turbine cascade located at Virginia Tech. This study was the culmination of all three previously studies. Again, the experimental set up will be covered first followed by the results and discussion.

5.A. INTRODUCTION

While spatially limited techniques such as, Laser Doppler Velocimetry (LDV) and Hot Wire Anemometry (HWA) have been very useful in understanding complex high speed flows without whole-field quantitative information, an instantaneous velocity characterization of the flow field cannot be made [44]. In order to understand time resolved coherent structure interaction, a total instantaneous flow field must be measured. Digital Particle Image Velocimetry (DPIV) provides instantaneous flow field measurements and has been used extensively for low sampling rate time average or phased locked measurements [45]. Due to a number of limitations, the use of DPIV with kHz sampling rates capable of accurately resolving high speed compressible flows.

Performing Time-Resolved Digital Particle Image Velocimetry (TRDPIV) in high speed wall bounded flows with high resolution/magnification often posses significant difficulties. However it can be particularly challenging in a high back pressure environment such as those found in a transonic turbine cascade tunnels. High pressure, high speed and the turbine blade complex geometries (high curvature and acceleration) significantly affect our ability to deliver homogeneous distribution of flow tracers, especially in the near wall region.

The work presented herein provides the results of a preliminary proof of concept experimental effort aimed to tackle the aforementioned difficulties. Two issues with this experiment are of particular interest. First, a seeder was specifically designed for this experiment in order to overcome the high pressure and provide sufficient volume flow rate of flow tracers. However, spatial and temporal variations of seeding density are always present and are increasingly evident when the flow is sampled with kHz rates. As a result the DPIV signal to noise ratio is compromised and regions with insufficient seeding result in extensive areas of bad vectors. In order to compensate for this effect, a gappy data reconstruction technique based on Proper Orthogonal Decomposition was developed and implemented to reconstruct the missing portions of the flow for each instantaneous flow field.

5.B. EXPERIMENTAL SETUP

Experiments inside the transonic turbine cascade where preformed as originally proposed. Here flow enters a turbine cascade that designed to replicate the first stage of a gas turbine. The flow enters at Mach 0.2 or 80 m/s and exits Mach 0.8. A square bar turbulence grid upstream of the test section is used to generate 12% free stream

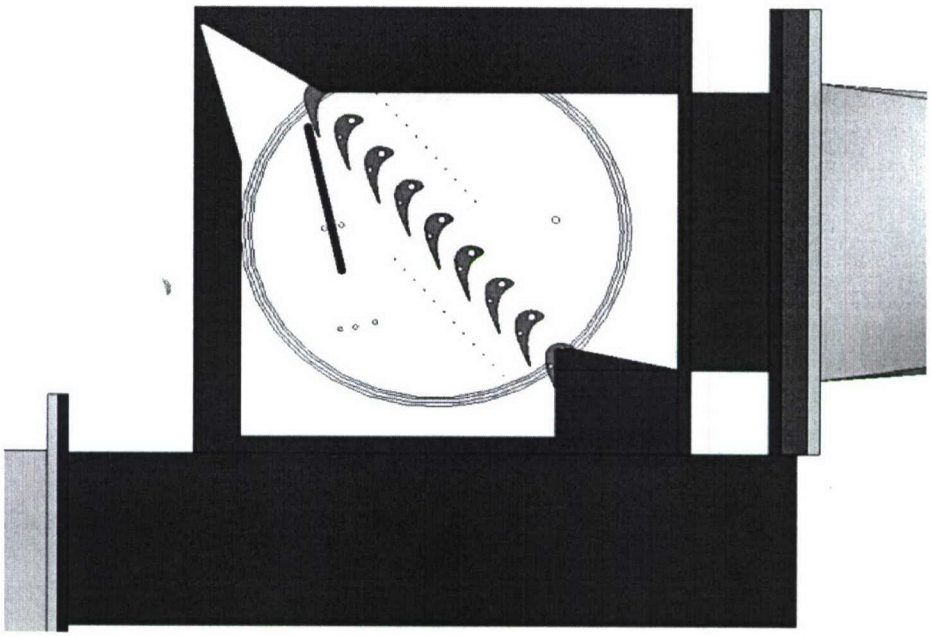
turbulence. The turbulence gird bar spacing and width where both 0.75 inches. The turbulence characteristics where found using at hot wire. This turbine cascade is well characterized and has been used for many projects where high speed high compression flow is desired. Pressure taps along the pitch of the cascade are used to characterize the inlet flow while a pitot tube is used to measure static and dynamic pressure inside the center of the tunnel. Tunnel Temperature is also recorded at the inlet in order to fully characterize the flow. Only this one flow condition was tested at the stagnation region of the center blade of a transonic cascade was studied. The turbine blade cord length was 2.75 inches.

All measurements in this study were preformed with Time Resolved Digital Particle Image Velocimetry (TR-DPIV) using a kHz Nd:YAG dual head laser. The use of a dual head laser allows for a reduction in the laser pulse separation to values as low as 50 ns. This capability is imperative to allow for high magnification measurements to be taken at high speeds. The laser plane was delivered through a glass window directly above the center blade illuminating the top and in front of the blade but did not allow for illumination underneath the blade as shown in Figure 32. A Photron Ultima APX-RS digital camera capable of sampling at 2500,000 frames per second was utilized for data collection. The resolution for this study was set to 1024x512 which allowed for a flow sampling rate of 3kHz. A pulse separations was calculated and was determined to be 3μs based on the ¼ rule imposed by the DPIV optimum interrogation window size with a magnification of 55 microns/pixel. The inlet velocity was 80 m/s resulting in a Reynolds number 266,000, based on cord length.

All TRDPIV images were processed using an in-house PIV code and utilized a Robust Phase Correlation (RPC) technique [9] coupled with a second-order discrete window offset technique [37]. The RPC method provided higher accuracy over standard cross correlation techniques by using dynamic phase-only filters along with an a priori spectral energy filter. It also has the advantage of greatly reducing peak-locking effects versus standard cross-correlation techniques.

In order to generate seed in a high speed high back pressure environment such as this, a new seeder was designed. The seeder again used a Laskin nozzle submerged in Diethylhexel sebacate (DHS), but this time the seeder was constructed so that the particle generation chamber could be pressurized above the working tunnel pressure. Figure 33 shows an exploded view of the new seeder with all of its major components labeled. The estimated droplet size was 1.0μm. Considering the fluid properties, we estimated that the Stokes number was on the order of $1x10^{-3}$ for a velocity of 80 m/s. It was with the creation of this seeder that project was able to make great progress forward when compared to the research done the previous year. While this addition produced improvements over previous trials, an inability to uniformly seed the test section required the use of the gappy reconstruction methodology described in section 3.

A)



B)

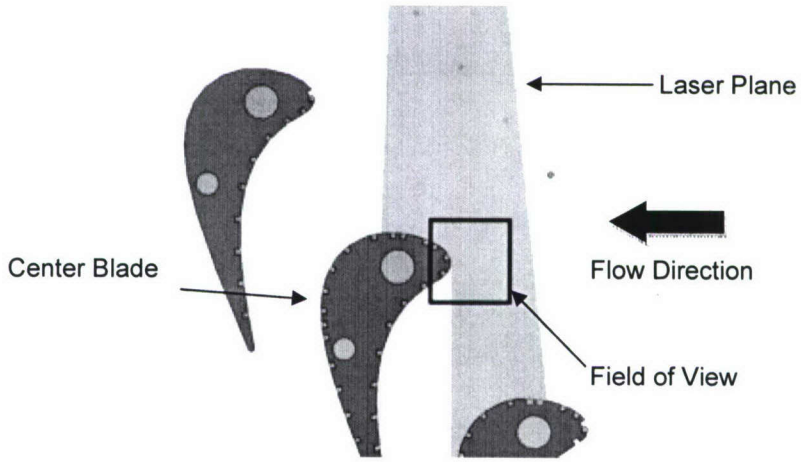


Figure 32. Diagram of the cascade configuration. A) shows blade orientation with respect to incident flow while B) shows laser placement and the shadow created do to optical constraints.

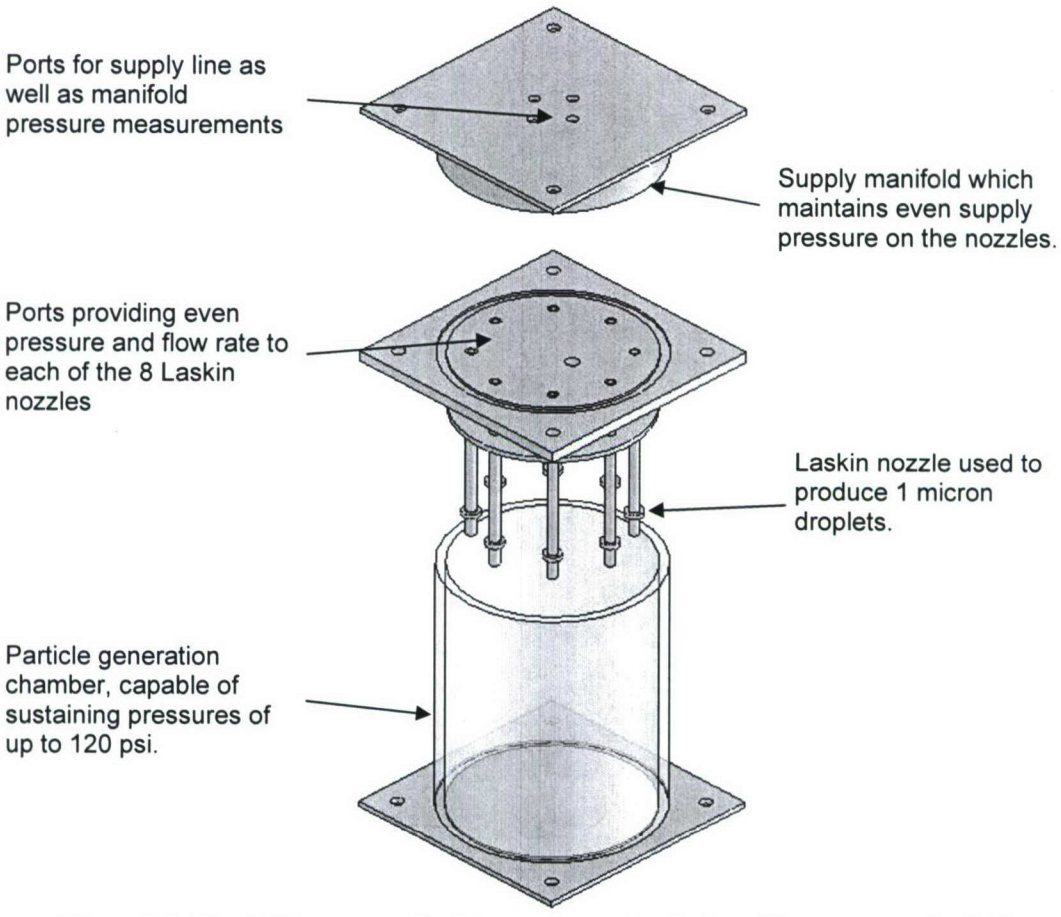


Figure 33. New high pressure Laskin nozzle seeder designed to overcome the high working pressure of the transonic cascade tunnel.

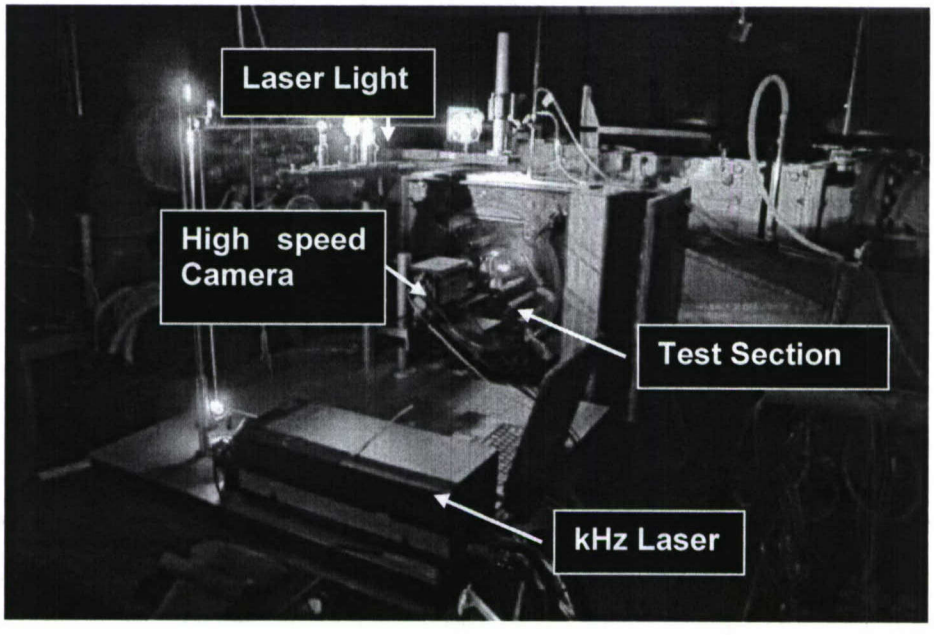


Figure 34. Demonstration of fully operation experimental setup..

5.C. RESULTS

As mentioned, due to the high working pressure and high speed found in the transonic tunnel, an inability to uniformly seed the region on interest produced gaps randomly in some of the images. These gaps produced areas of incorrect velocity and had to be removed and replaced. As discussed in section 2, a Proper Orthogonal (POD), based reconstruction method was applied to the data to help replace areas lost due to these gaps. Figure 34 shows two different instantaneous snap shot (A,B) where low seeding density was present and a flow field showing the resulting loss of correlation (C).

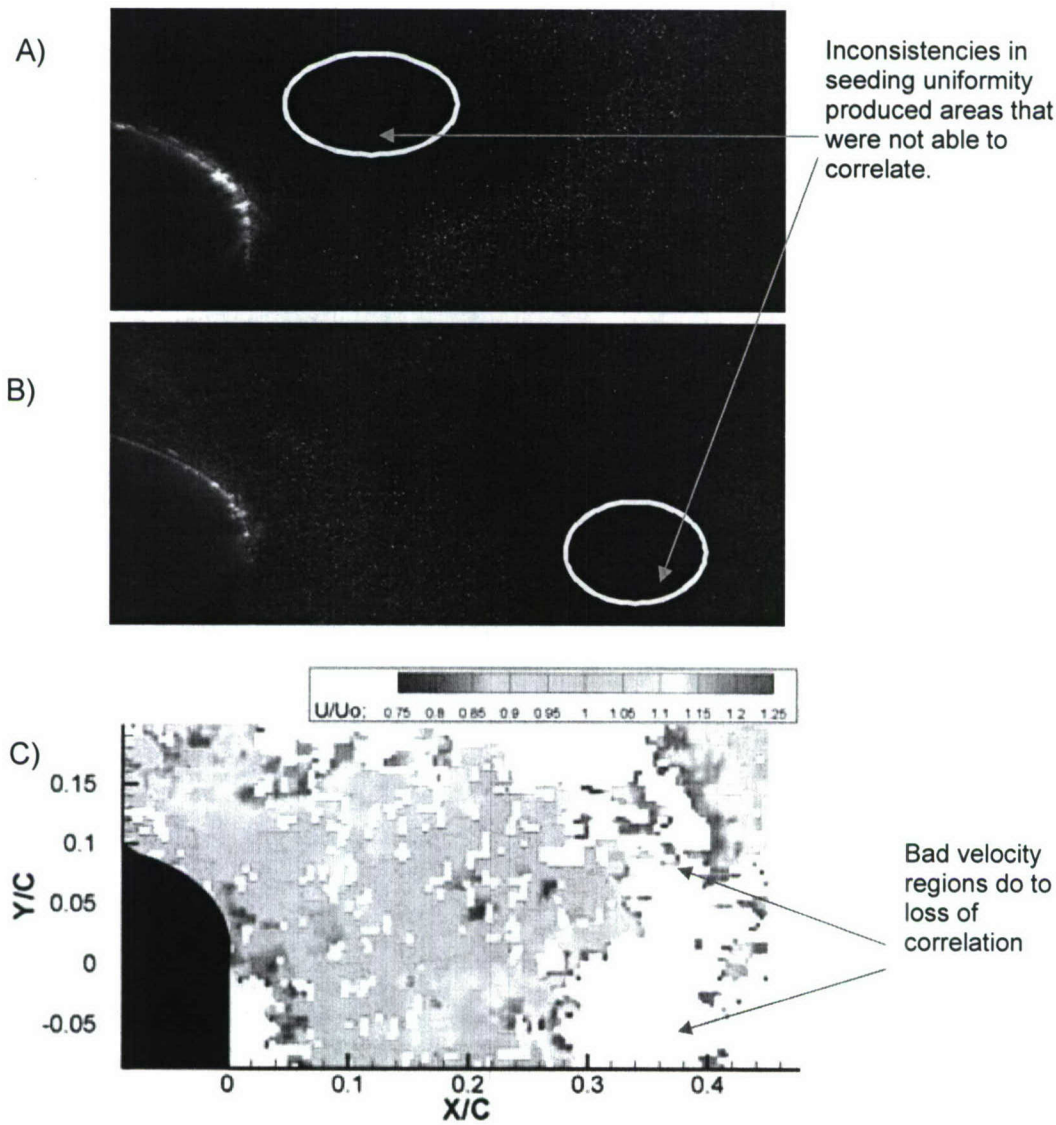


Figure 34. Instantaneous camera images show areas of low seeding density and a corresponding velocity field illustrating the loss of correlation. The (0,0) point in C) locates the stagnation point

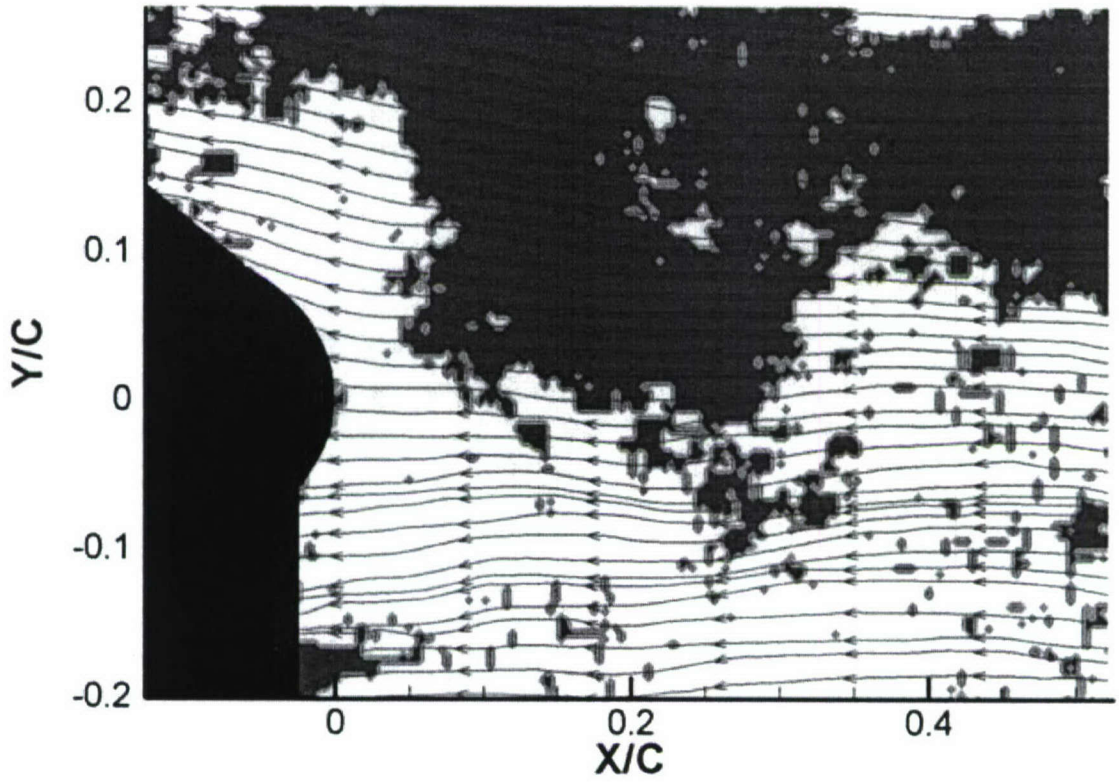


Figure 35. Here an extreme case of low seeding is shown in blue with the instantaneous stream lines of the reconstructed flow field shown over top.

Through the utilization of the POD reconstruction previously discussed, instantaneous fields that where previous unusable are not contributing pieces of data. Figure 35 shows an extreme case where almost 50% of the instantaneous field was corrupted due to low seeding. The streamlines in this figure show the reconstructed velocity direction. While this specific frame was subject a high loss of correlation, this was not the average but it did provide a good example for the power of the newly developed POD reconstruction.

This experiment has also shown the ability to capture instantaneous vortices in the upstream section of the turbine cascade. Figure 37 shows an instantaneous vortex generated from the turbulence grid moving towards the stagnation region. The vortex identification method described in section 4.E. was also applied to this field. Figure 36 shows the location of a few of the vortices located throughout the test section. This figure helps to validate the hypothesis that the grid up stream of the test section is generating homogeneous turbulence. This identification method will be instrumental if future work is to be done on the study of blade vortex interaction and their effects on heat transfer.

A preliminary investigation of frequency information was also preformed. Similar to the analysis preformed in section 4.F, a Power Spectral Density was performed on the temporal POD coefficients. This analysis again shows that most dominant temporal

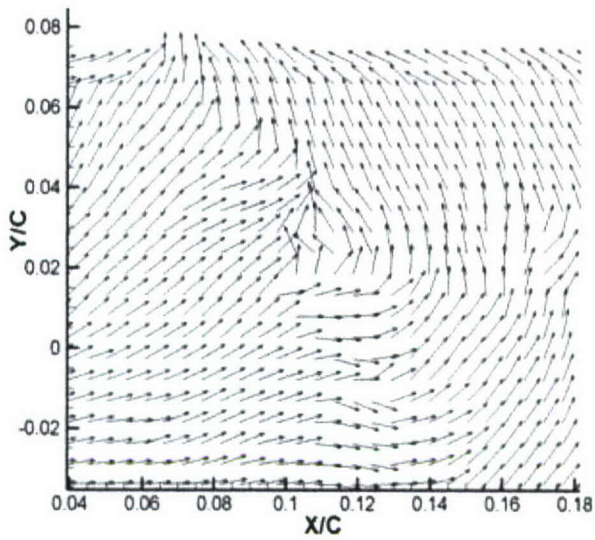


Figure 37 This is an instantiations shot of a vortex moving approaching the stagnation point. The average velocity has been subtracted off. The axis is normalized so that (0,0) is the

information is contained in the lower, higher energy modes. A previous study preformed in this cascade with a similar turbulence generator (bar grid with a bar dimension of 0.80 inches) has shown that generated vortices have a dominate frequency between 600 and 700 Hz [46]. This is in good agreement with the results shown in Figure 38. This demonstration helps to further validate the time resolved nature of the results obtained in this study.

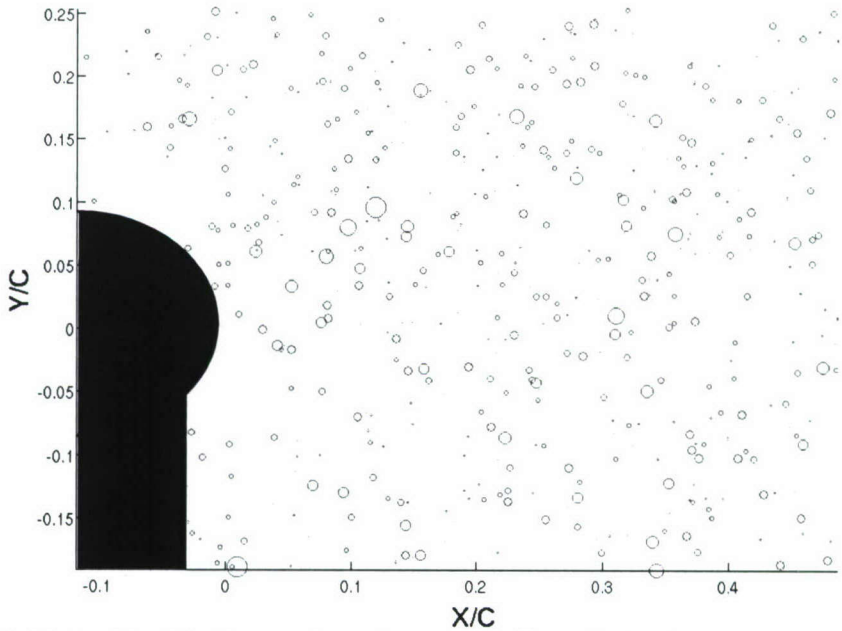


Figure 36. Vortex identification as shown in section 4.E. applied to instantaneous cascade data. Circle Size is a measure of circulation normalized with maximum circulation value found.

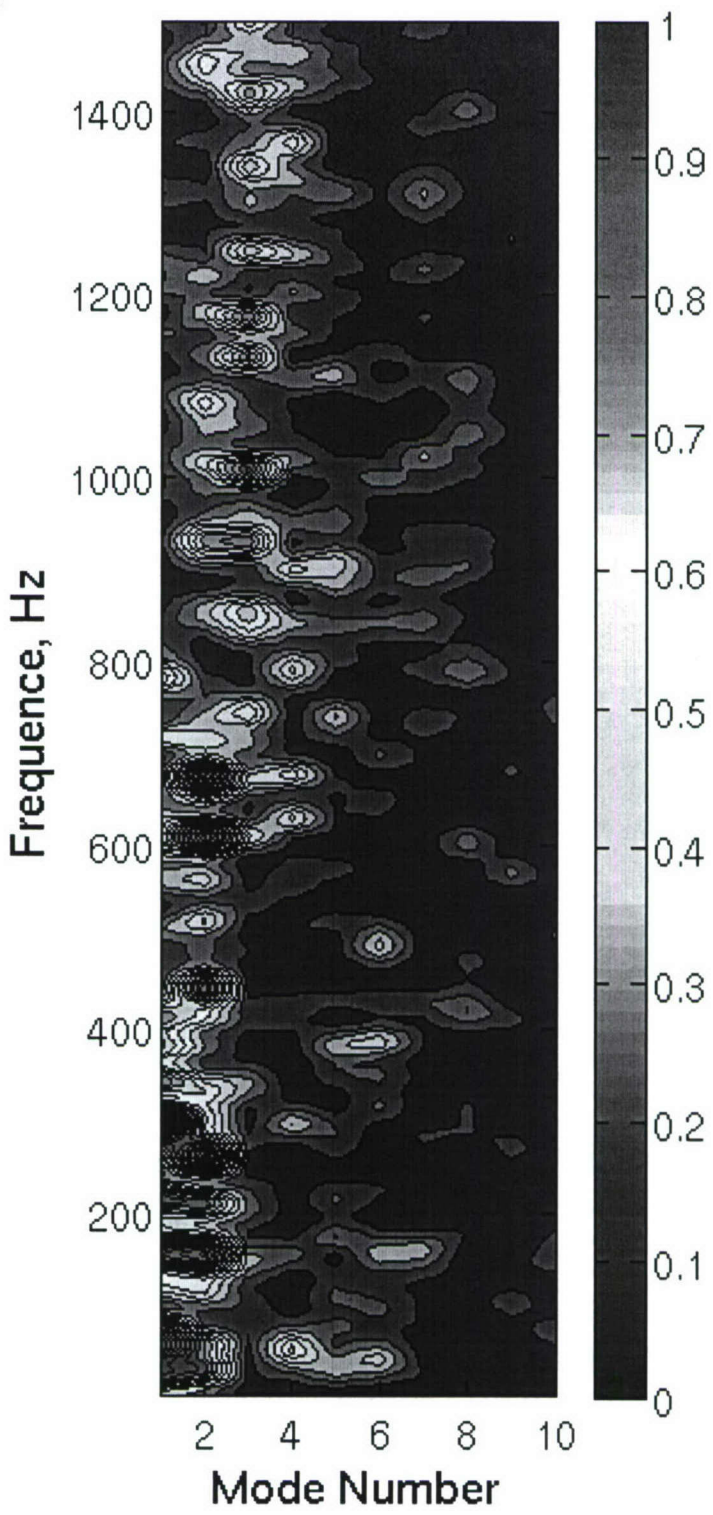


Figure 38. Contour plots of spectral density for the temporal coefficient produced from POD. The contour shows power for each individual frequency normalized against the maximum value for the total spectrum.

5.D. CONCLUSIONS

Through the development of both methodology and physical equipment, this work has demonstrated that Time Resolved Digital Particle Image Velocimetry is possible inside of a transonic turbine cascade. The use of a high pressure Laskin nozzle seeder, which greatly improved capability over previous trials, was insufficient by itself to make these measurements possible. It was only with the addition of an advanced data reconstruction technique that time resolved instantaneous flow fields where captured. This work will be instrumental in future studies of not only flow field statistics and boundary layer development but there influence on transfer as well.

6. CONCLUSIONS AND FUTURE WORK

During the two year time frame of this project a successful demonstration of high frequency, high magnification near wall Time Resolved Digital Particle Image Velocimetry measurements in a transonic cascade was accomplished. Preliminary studies performed in this time framed helped to fully understand difficulties inherent to measurements in side of a high speed high back pressure environment. To this end, the development of both a high pressure particle generator and an advanced data reconstruction methodology was developed. While the development of the particle generator alone was able to advance this study much further than previous trials, it was in conjunction with the reconstruction methodology that the best results were produced. With these developments a more in depth investigation of flow characteristics can be undertaken. Future work will now be able to study the interaction of large scale turbulent structures on the stagnation region of a transonic cascade blade and the resulting effect on heat flux and over all blade temperature.

7. REFERENCES

[1] Radomsky RW, and Thole KA, (2000) *Flowfield Measurements for a Highly Turbulent Flow in a Stator Vane Passage," J. of Turbomachinery*, **22:**255-262

[2] Radomsky RW, and Thole KA (2002) *Detailed Boundary Layer Measurements on a Stator Vane at Elevated Freestream Turbulence Levels," J. Turbomachinery*, **124**:107-118.

[3] Murray NE, Ukeiley LS (2007) *An Application of Gappy POD.* Exp Fluids. **42**:79-91.

[4] Gunes H, Sirisup S, Karniadakis GE (2006) *Gappy Data: To Krig or not to Krig?* J Comp Phys **212**:358-382.

[5] Nogueira J, Lecuona A, Rodriguez P (1997) *Data Validation, False Vectors Correction and Derived Magnitudes Calculation on PIV Data.* Meas Sci Technol **8**: 1493-1501.

[6] Vedula, P, Adrian RJ (2005) *Optimal Solenoidal Interpolation of Turbulent Vector Fields: Application to PTV and Super-Resolution PIV.* Exp Fluids **39**: 213-221.

[7] Hart DP (1998) *The Elimination of Correlation Errors in PIV.* Processing, in 9th International Symposium on Applications of Laser Techniques to Fluid Mechanics. Lisbon, Portugal 1998.

[8] Westerweel J (1994) *Efficient Detection of Spurious Vectors in Particle Image Velocimetry Data.* Exp Fluids **16**:236-247.

[9] Eckstein A, Vlachos PP (2007) *A Robust Phase Correlation DPIV. Processing Algorithm for Time Resolved Measurements*, in *PIV Symposium*. Rome, Italy.

[10] Fore LB, Tung AT, Buchanan JR, Welch JW (2005) Nonlinear Temporal Filtering of Time-Resolved Digital Particle Image Velocimetry Data. Exp. Fluids **39**:22-31

[11] Oliver MA and Webster R (1990) *Kriging: A Method of Interpolation for Geographical Information Systems.* Int J Geograph Inf Sys **4**(3):313-332.

[12] Druault P, Chaillou C (2007) *Use of Proper Orthogonal Decomposition for Reconstructing the 3D in-Cylinder Mean-Flow Field From PIV Data.* Comptes Rendus Mecanique **335**:42-47.

[13] Everson R, Sirovich L (1995) *Karhunen-Loeve Procedure for Gappy Data.* J of Opt Soc of Am **12**(8):1657-1664.

[14] Venturi D (2006) *On Proper Orthogonal Decomposition of Randomly Perturbed Fields with Applications to Flow Past a Cylinder and Natural Convection Over a Horizontal Plate.* J Fluid Mech **559**:215-254.

[15] Venturi D,Karniadakis GE (2004) *Gappy Data and Reconstruction Procedures for Flow Past a Cylinder.* J Fluid Mech **519**:315-336.

[16] Stanislas M, Okamoto K, Kahler CJ, Westerweel J. (2005) *Main Results of the Second International PIV Challenge.* Exp Fluids. **39**: 170-191.

[17] Sirovich L (1989) *Chaotic Dynamics of Coherent Structures.* Physica D **37**:126-145.

[18] Zoldi SM, Greenside HS (1997) *Karhunen-Loeve Decomposition of Extensive Chaos.* Phys Rev Let **78**(9).

[19] Sirovich L (1987) *Turbulence and the Dynamics of Coherent Structures I-III.* Quart App Math **45**:567-571.

[20] Ma X., Karniadakis GE, Park H, and Gharib M, (2003) *DPIV - Driven Flow Simulation: A New Computational Paradigm*. Proc R Soc. **459**: 547-565.

[21] Gunes H, Rist U (2007) *Spatial Resolution Enhancement/Smoothing of Stereo–Particle-Imagevelocimetry Data using Proper-Orthogonal-Decomposition–Based and Kriging Interpolation Methods.* Phys Fluids **19**:1-19.

[22] Launder BE, and Rodi W (1983) *The Turbulent Wall Jet – Measurements and Modeling*, Ann Rev Fluid Mech **15**:429-459.

[23] Chiriac, VA and Ortega A (2002) *A Numerical Study of the Unsteady Flow and Heat Transfer in a Transitional Confined Slot Jet Impinging on an Isothermal Surface*. Int. J of Heat & Mass Trans. **45**: p. 1237-1248.

[24] Barenblatt GI, Chorin AJ, and Prostokishin VM, (2005) *The Turbulent Wall Jet: A Triple-Layered Structure and Incomplete Similarity.* Proceedings of the National Academy of Sciences,. **102** (25).

[25] Durbin P, and Wu X (2007) *Transition Beneath Vortical Disturbances.* Ann. Rev. of Fluid Mech. **39**: p. 107-128.

[26] Williams DR, Fasel HF, and Hama FR (1984) *Experimental Determination of the Three-Dimensional Vorticity Field in the Boundary Layer Transition Process.* J Fluid Mech. **149**: p. 179-203.

[27] Chun DH, Schwarz (1967) *Stability of the Plane Incompressible Viscous Wall Jet Subjected to Small Disturbances*, Phys. Fluids **10:**991

[28] Amitay M, Cohen J (1997) *Instability of a Two-Dimensional Plane Wall Jet Subjected to Blowing or Suction*, J. Fluid Mech **334**:67-94.

[29] Schneider ME, Goldstein RJ (1994) *Laser Doppler Measurement of Turbulence Parameters in a Two-Dimensional Plane Wall Jet*, Phys. Fluids **6**(9):3116-3129.

[30] Bajura RA, Catalano R (1975) *Transition in a Two-Dimensional Plane Wall Jet*, Fluid Mech. **70**:773-799.

[31] Gegineni S, Visbal M, Shih C (1999) *Phase-Resolved PIV Measurements in a Transitional Plane Wall Jet: A Numerical Comparison*, Exp. Fluids, **27**:126-136.

[32] Gogineni S, Shih C (1997) *Experimental Investigation of the Unsteady Structure of a Transitional Plane Wall Jet*, Exp Fluids, **2**:121-129.

[33] Berkooz G, Holmes P, Lumley JL (1993) *The Proper Orthogonal Decomposition in the Analysis of Turbulent Flows*, Ann. Rev. Fluid Mech. **25**:530-575.

[34] Sirovich L (1987) *Turbulence and the Dynamics of Coherent Structures I-III.* Quart App Math **45**:567-571.

[35] Aubry N, Holmes P, Lumley JL, Stone E (1988) *The Dynamics of Coherent Structures in the Wall Region of a Turbulent Boundary Layer*, J. Fluid Mech. **192**:115-173.

[36] Delville J, et al. (1999) *Examination of Large-Scale Structures in a Turbulent Plane Mixing Layer. Part 1. Proper Orthogonal Decomposition.* J Fluid Mech, 1999. **391**: p. 91-122.

[37] Scarano F, Riethmuller ML (1999) *Iterative Mutigrid Approach in PIV Image Processing with Discrete Window Offset*, Exp Fluids **26**:513-523.

[38] Everson R, Sirovich L (1995) *Karhunen-Loeve Procedure for Gappy Data,* J of Opt Soc of Am 12(8):1657-1664.

[39] Sirovich L (1989) *Chaotic Dynamics of Coherent Structures,* Physica D 37:126-145.

[40] Zoldi SM, Greenside HS (1997) *Karhunen-Loeve Decomposition of Extensive Chaos.* Phys Rev Let 78(9).

[41] Jeong J, HussainF, (1995) *On the Identification of a Vortex*, J. Fluid Mech. **285**:69-94.

[42] Hall JW, Ewing D (2007) *Three-Dimensional Turbulent Wall Jets Issuing from Moderate-Aspect-Ratio Rectangular Channels*, AIAA J. **45**(6):1177-1185.

[43] Levin O, Chernoray VG, Lofdahl L, Henningson DS (2005) A Study of the Blasius Wall Jet, J. Fluid Mech. **539**:313-347.

[44] Humble RA, Scarano F, van Oudheusden BW (2007) *Particle Image Velocimetry Measurements of a Shock Wave/Turbulent Boundary Layer Interaction*, Exp Fluids. **43**:173-183.

[45] Adrian RJ (2005) Twenty Years of Particle Image Velocimetry, Exp. Fluids. **39**:159-169

[46] Nix AC, Diller TE, Ng WF (2004) *Experimental Measurements and Modeling of the Effects of Large-Scale Free Stream Turbulence on Heat Transfer*, Proceedings of ASME Turbo Expo, June 14-17, Vienna, Austria